Electrical joints optimized for increased thermal and mechanical fatigue life

Public report

Project within Circularity - FFI - Juni 2022
Authors Tag Hammam, Ethan Sullivan, Peter Andersson, Adrianna Lozinko, Oliwer Gustavsson, Babak Ghazian, David Löveborn, David Malmström, Alexander Lundstjälk, Love Englund, Nader Heshmati and Jukka-Pekka Anttonen
Date 2025-08-29

Content

FFI in short

FFI, Strategic Vehicle Research and Innovation, is a joint program between the state and the automotive industry running since 2009. FFI promotes and finances research and innovation to sustainable road transport.

For more information: www.ffisweden.se

1. Summary

The aim of this study was to develop a new testing methodology for investigation of thermal and mechanical fatigue in laser welded busbar-tab electrical connections for prismatic battery cells. Additionally, evaluation of permanent electrical connections for other applications is included in this study to broaden the use of the developed test method.
A fatigue test rig was developed to perform fatigue test under constant current load, as well as a test coupon was proposed to mimic the laser welded aluminum connection in a prismatic battery. In general, detection of fatigue damage via the force-displacement loop was more accurate than via measurement of the voltage drop. In some cases, the voltage drop could be correlated with the presence of fatigue damage, but this correlation was typically not consistent. High-resolution X-ray computed tomography (CT) was an effective method for detecting welding defects such as gas pores or solidification cracks.
Overall, most of the samples survived the fatigue testing despite the exaggerated load amplitude used, despite the presence of initiation points for fatigue damage, e.g. cracks at the end crater, and pores in the weld.
3D CT scan revealed pores in many of the as-welded samples. Most notably, annealing (350 °C, 1 hour) combined with a small gap resulted in almost pore-free welds. The soft-annealed samples survived for a high-cycle severe fatigue testing at very high-load amplitude despite a less-than-optimal microstructure caused by the annealing (i.e. significant recrystallization and grain growth). Moreover, in real battery applications, soft annealing of the busbars combined with a bend in the middle of the busbar may reduce the mechanical stress experienced by the joint during operation.
Mechanical fatigue under applied constant current load of 300 A DC resulted in an increase of the test sample in temperature typically between 40 °C – 60 °C depending on the weld geometry. However, this did not significantly reduce the fatigue life length. Even a test sample heat-treated for 1 month at 120 °C to simulate the effect of elevated temperature due to the electric current survived a high-cycle severe fatigue testing at very high load amplitude, even though the fatigue life length was somewhat reduced compared to a non-heat-treated sample.
In most laser welding cases, the laser power was abruptly switched off at the end of the weld which resulted in the formation of an end crater depression and solidification cracks in the end crater, which acted as initiation points for fatigue damage. Oxidation of test samples in a climate chamber was performed to simulate one year storage at 100% RH.
The oxide layer thickness increased from approximately 2 -3 nm to approximately 9 - 10 nm, which contributed to the formation of larger pores at the sides of the weld, which is likely undesirable for fatigue performance.

Laser welding with different weld shapes clearly demonstrated that the weld geometry plays a large role in dictating where cracks initiate and propagate. In the linear welds, cracks were nearly always found to initiate at solidification cracks in the end crater and then propagated along the weld length while remaining wholly in the 1050 tab material.

Decreased weld width from 1.0 mm to 0.7 mm in linear welds had a noticeable, detrimental effect on fatigue performance. Laser welding of different Al alloys resulted in a higher extent of solidification cracking in the end crater and in the steady-state portion of the weld was observed in 6101-3003 laser-welded samples.

Resistance welded tin coated copper busbars were produced to investigate the effect of the thickness of the tin coating. The optimum tin coating thickness is probably in the range of 1 – 3 µm. For coating thicknesses above 3 µm, the thickness of the intermetallic compound formed during welding was almost the same regardless of the thickness of the tin coating. Therefore, thicker coatings potentially being used in production could be reduced to 3 µm or lower to reduce costs. Further work is required to fully understand the interplay of the original coating thickness and the resistance welding parameters and their effect on the intermetallic layer thickness. Despite the presence of fatigue damage, the resistance welded tin coated copper withstood severe fatigue test for an intermediate cycle fatigue test at a high load amplitude (2 Mcycles, 60 N load amplitude). Furthermore, experiments of resistance welding copper to copper busbars without tin coating, but with stamped projections were performed but failed to achieve a tensile strength similar to that of the tin-coated samples, probably due to premature collapse of the dimples during welding.

Finally, a guideline for welding of electrical joints based on the findings of this work was developed.

2. Sammanfattning på svenska

Syftet med denna studie var att utveckla en ny testmetodik för undersökning av termisk och mekanisk utmattning i lasersvetsade elektriska anslutningar mellan aluminiumskenor och batteriterminalen för prismatiska battericeller. Dessutom ingick utvärdering av permanenta elektriska anslutningar för andra tillämpningar i denna studie för att bredda användningen av den utvecklade testmetoden.

En utmattningstestrigg utvecklades för att utföra utmattningstest under konstant strömbelastning, samt en testkupong föreslogs för att efterlikna den lasersvetsade aluminiumanslutningen i ett prismatiskt batteri. I allmänhet var detektering av utmattningsskador via kraft-lägesloopen mer exakt än via mätning av spänningsfallet. I vissa fall kunde spänningsfallet korreleras med förekomsten av utmattningsskador, men denna korrelation var vanligtvis inte konsekvent. Högupplöst röntgendatortomografi (CT) var en effektiv metod för att detektera svetsfel såsom gasporer eller stelningssprickor. Sammantaget överlevde de flesta proverna utmattningstestet trots den överdrivna belastningsamplituden som användes, trots förekomsten av initieringspunkter för utmattningsskador, t.ex. sprickor vid ändkratern och porer i svetsen. 3D-CT-skanning avslöjade porer i många av de svetsade proverna. Ett intressant resultat var att glödgning (350 °C, 1 timme) i kombination med ett litet mellanrum resulterade i nästan porfria svetsar. De mjukglödgade proverna överlevde ett högcykliskt utmattningstest vid mycket

hög belastningsamplitud trots en mindre optimal mikrostruktur orsakad av glödgningen (dvs. betydande omkristallisation och korntillväxt). Dessutom kan mjukglödgning av aluminiumskenorna i kombination med en böjning i mitten av aluminiumsken i verkliga batteriapplikationer minska den mekaniska belastningen som fogen upplever under drift.

Mekanisk utmattning under applicerad konstantströmsbelastning på 300 A DC resulterade i en temperaturökning hos testprovet, vanligtvis mellan 40 °C och 60 °C, beroende på svetsgeometrin. Detta minskade dock inte utmattningslivslängden signifikant. Även ett testprov som värmebehandlats i 1 månad vid 120 °C för att simulera effekten av förhöjd temperatur på grund av den elektriska strömmen överlevde ett högcykliskt utmattningstest vid mycket hög belastningsamplitud, även om utmattningslivslängden minskades något jämfört med ett icke-värmebehandlat prov.
I de flesta fall av lasersvetsning stängdes lasereffekten abrupt av i slutet av svetsen, vilket resulterade i bildandet av en fördjupning i ändkratern och stelningssprickor i ändkratern, vilka fungerade som initieringspunkter för utmattningsskador. Oxidation av testprover i en klimatkammare utfördes för att simulera ett års lagring vid 100 % RF. Oxidskiktets tjocklek ökade från cirka 2–3 nm till cirka 9–10 nm, vilket bidrog till bildandet av större porer vid svetsens sidor, vilket sannolikt är oönskat för utmattningsprestanda.

Lasersvetsning med olika svetsformer visade tydligt att svetsgeometrin spelar en stor roll för att diktera var sprickor initieras och fortplantar sig. I de linjära svetsarna fann man att sprickor nästan alltid initierades vid stelningssprickor i ändkratern och sedan fortplantade sig längs svetslängden medan de helt förblev i 1050-flikmaterialet. Minskad svetsbredd från 1,0 mm till 0,7 mm i linjära svetsar hade en märkbar, skadlig effekt på utmattningsprestanda. Lasersvetsning av olika Al-legeringar resulterade i en högre grad av stelningssprickbildning i ändkratern och i den stationära delen av svetsen observerades i 6101-3003 lasersvetsade prover.

Motståndssvetsade tennbelagda kopparskenor tillverkades för att undersöka effekten av tennbeläggningens tjocklek. Den optimala tennbeläggningstjockleken ligger förmodligen i intervallet 1–3 µm. För beläggningstjocklekar över 3 µm var tjockleken på den intermetalliska föreningen som bildades under svetsningen nästan densamma oavsett tennbeläggningens tjocklek. Därför skulle tjockare beläggningar som potentiellt kan användas i produktionen kunna minskas till 3 µm eller lägre för att minska kostnaderna. Ytterligare arbete krävs för att fullt ut förstå samspelet mellan den ursprungliga beläggningstjockleken och motståndssvetsparametrarna och deras effekt på det intermetalliska skiktets tjocklek. Trots förekomsten av utmattningsskador motstod den motståndssvetsade tennbelagda kopparn ett hårt utmattningstest för ett mellanliggande cykelutmattningstest vid en hög belastningsamplitud (2 Mcykler, 60 N belastningsamplitud). Dessutom utfördes experiment med motståndssvetsning av koppar till kopparskenor utan tennbeläggning, men med formpressade förhöjningar, men misslyckades med att uppnå en draghållfasthet liknande den för de tennbelagda proverna, troligen på grund av för tidig kollaps av de formpressade förhöjningar under svetsningen.

Slutligen utvecklades en guideline för svetsning av elektriska fogar baserad på resultaten från detta arbete.

3. Background

Electromobility is currently one of the largest factors pushing further development of battery cells for energy storage[1]. In electrical vehicles, several individual battery cells are joined or welded to each other in series or parallel along a busbar to form a battery pack. Battery cells exist in multiple geometries (Figure 1), where the largest type is the prismatic cell and is the focus of this study.

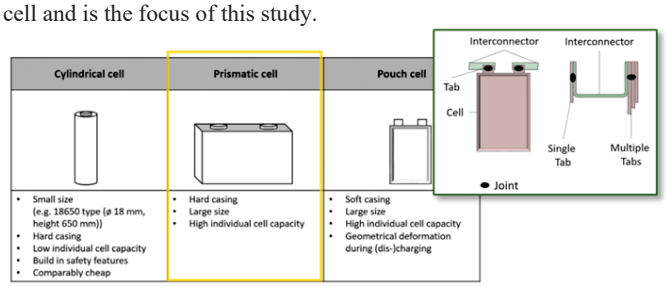

Figure 1 Schematic representations of three types of battery cell where the prismatic cell is of interest in this project. An inset of the welded busbar-tab connections is shown. Adapted from [2].

Welded battery cell joints are subjected to an extremely complex combination of mechanical and thermal loads during service, including dynamic loading and random vibrations due to vehicle motion, residual stress imparted by the welding process, and cyclical thermal loading in which elevated temperatures can be experienced due to the electrical current flowing through the weld. Heating of the joint increases the electrical resistance across the joint, which in turn increases the temperature, creating a detrimental feedback loop leading to thermal runaway that can potentially cause damage to the battery. As such, a large variety of factors must be accounted for to accurately predict the long-term performance and durability of the battery. Figure 2 shows an example of the complex interplay of thermal loading parameters and electrical properties (ignoring mechanical loads) that affect the performance degradation of the battery.

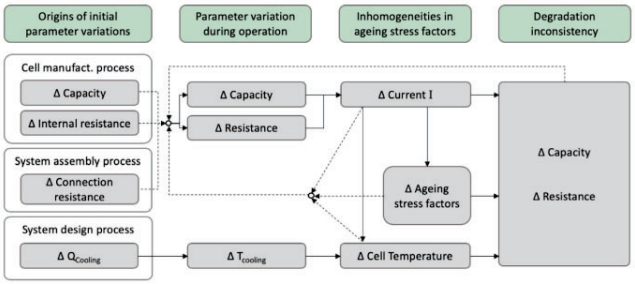

Figure 2 Map of thermal load and electrical property parameters that affect the performance degradation of a battery cell[3].

Several different methods are employed today to join battery cells, including laser welding, ultrasonic welding, micro-gas tungsten arc welding, and resistance spot welding. Laser welding can give lower electrical contact resistance compared to ultrasonic or spot welding (see Figure 3), and laser welding involves relatively limited heat input over a narrow area, which is important to not damage or degrade the battery materials near where the welding is done[4]. One laser welding case study, for example, measured temperatures reaching 87 °C at the cell terminal and 33 °C at the cylinder barrel[5]. Laser welding in general presents potential challenges, including formation of porosity, lack-of-fusion defects, difficulties in welding reflective materials, and small gap tolerances requiring clamping. These challenges naturally apply to laser welding of pure Al-Al, which is the focus of this project. Laser welding of dissimilar metal combinations like Cu-Al, for example, can introduce further complications, such as solidification cracking or the formation of brittle intermetallic compounds which are detrimental to the mechanical performance of the joint.

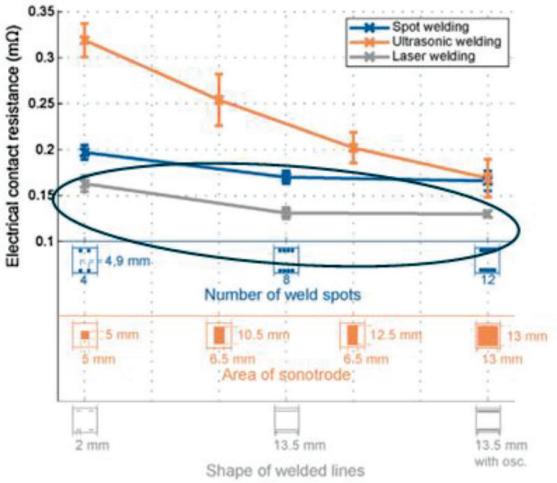

Figure 3 Electrical contact resistance vs. different welding parameters for resistance spot, ultrasonic, and laser welding of CuZn37 samples. Adapted from [5].

The large number of batteries that are connected in series in a vehicle result in ultra-high demand for each joint, typically a failure rate of 1 in five million or less is acceptable (based on 250 batteries per vehicle x 2 battery terminals per battery and an acceptable failure rate per vehicle of 1 in 10000). This in combination with requirements of very short cycle time for the laser welding process and that the temperature on the rear side of the battery terminal needs to be restricted to be in the range of 80 °C to 100 °C, makes the laser welding of battery terminals very challenging.

Given the complexity of the problem, adequate and complete testing methodologies do not currently exist for examining the effect of thermal and mechanical loads on the fatigue life of these types of welded battery cell joints. Therefore, this study was conceived as part of a project aiming to develop a new testing methodology for investigation of thermal and mechanical fatigue in welded busbar-tab electrical connections in prismatic battery cells. Additionally, evaluation of permanent electrical connections for other applications was included in this study to broaden the use of the developed test method. Thus, laser welded busbars of Al 1370 to 3003 and Al 6101 to 3003 as well as resistance welded tin coated copper busbars were included in this study.

4. Purpose, research questions and method

The aim of this study was to develop a new testing methodology for investigation of thermal and mechanical fatigue in laser welded busbar-tab electrical connections for prismatic battery cells. Additionally, evaluation of permanent electrical connections for other applications is included in this study to broaden the use of the developed test method.

Test approach for battery joints

The obvious way to test the battery joints would be to test the battery joints under simulated operating conditions and provided that the outcome is lower than the limit value for the acceptable failure rate, the battery joint process can be approved. However, since the acceptable failure rate is very high, typically a failure rate of 1 in five million or less, and it is not possible to test millions of battery joints during simulated operating conditions, a totally different test approach is needed. In this study we propose the following approach to ensure that the failure rate can be kept below the limit value:

1. Exaggerated mechanical fatigue testing to evaluate the effect of the laser pattern, laser process and so forth.
2. Evaluation of enhanced temperature on the fatigue properties
3. To investigate when laser defects occur and the consequences on the fatigue properties

Based on the results of the above proposed tests, measures can be taken to reduce the risk of catastrophic failures of the battery joints in the field.

5. Objective

The overall goal for the project was to increase the circularity and sustainability in the automotive industry by ensuring electrical joints subjected to thermal and mechanical fatigue are produced with high quality thus minimizing the risk of premature failures and reduced efficiency. The increased quality was reached by developing a method for practical evaluation and benchmarking of electrical connections subjected to thermal and mechanical fatigue. The method will ensure both decreased use of raw materials, through decreased number of failures in battery systems, and by enabling 2nd life opportunities of the battery pack. For manufacturers, a standardized test specimen will enable qualification of suppliers, materials, and techniques. The proposed methodology combining resistance measurements, fatigue testing & FE analysis can be utilized for the development of a guideline for how to design and optimize properties in electrical joints.

Technical Goals

- Developing a universal method for fast and precise measurements of contact resistance in welded electrical joints. The method should also be able to monitor contact resistance

variations for determination of crack initiation. This technique is commonly known as *Direct Current Potential Drop* (DCPD) but needs to be adapted for the application.
- Summarize state of the art techniques and requirements for welding electrical connections. Welding methods, material solutions and recycled alloys and environmental aspects should be included to help manufacturers choose the best method with lowest environmental impact.
- Defining degree of restraint and temperature cycles for busbars to be used as input for demonstrator and FEM simulation.
- Develop models for analysis of fatigue results from standardized specimens and utilize these for optimized design of busbars.
- Developing and verifying a fatigue testing method for standardized test specimens with the ambition to make it broadly adopted in the EV industry. The testing method will link the contact resistance, weld geometry, welding process/parameters and busbar geometry.
- With a demonstrator showing the full work methodology going from a CAD drawing of a busbar to verifying if the construction will reach targeted fatigue performance.

Sustainability/circularity Goals

- To ensure high performance of the electrical joints in the battery pack which will increase the power efficiency, reduce risk of breakdowns, and extend the lifetime of the vehicle.
- To minimize the carbon footprint of EVs by enabling long life and 2nd life opportunities of the battery pack.
- Enable manufacturers to maximize the lifetime of the product and review changes in the material, process, or geometry.
- Through the development of a new fatigue testing method enable manufacturers to compare, test and qualify recycled alloys for use in battery pack construction to increase circularity and minimize environmental impact.

6. Results and deliverables

Before performing fatigue testing as part of the main investigation, other tests were conducted to evaluate the performance of the fatigue test rig and to understand the magnitude of the temperature rise in the cross-samples subjected to high current. For this initial measurement of temperature at high current, a separate fixture was made (Figure 4).

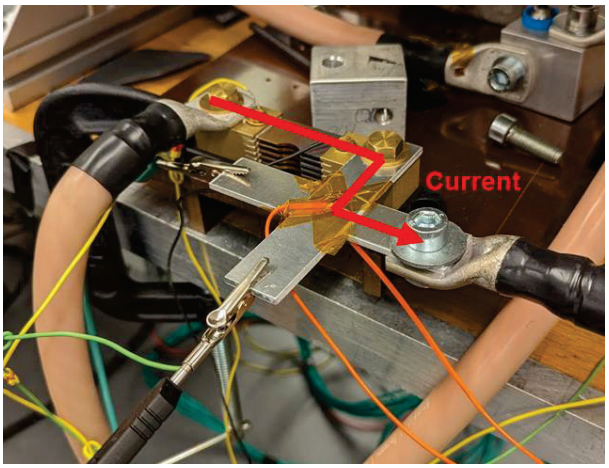

Figure 4 Fixture for applying high current and measuring temperature via thermocouples on the weld/front side and opposite side of a cross-sample.

Two different material combinations (6061 1.5 mm tab to 3003 3.2 mm busbar and 1050 1.2 mm tab to 3003 3.2 mm busbar) welded with and without Trumpf Brightline (a type of spot-in-ring laser beam shaping) and with a full or interrupted S weld shape were subjected to high currents in the range of 100 A up to 500 A in steps of 100 A. Typically, 30 minutes were allowed to elapse before stepping up to the next current level to allow steady state to be reached. If the temperature exceeded 160 °C, the test was aborted.
The results of this initial evaluation are shown in Figure 5. Higher maximum temperatures (145 °C-155 °C) at 500 A were observed in the material combination with the thinner 1050 tab compared to 120 °C in the 6101 material combination. Additionally, the interrupted S weld did not result in any significant difference in maximum temperature compared to the other 1050 material combination welds.

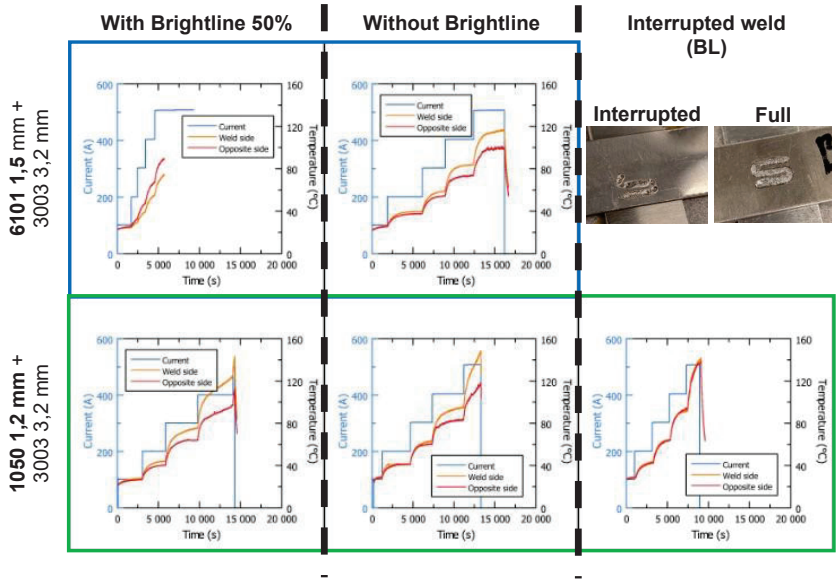

Figure 5 Temperature and current vs. time for the different material combinations and weld strategies performed for the initial evaluation of heat evolution in the cross-samples.

The same samples with Brightline and the full weld shape (i.e., those in the leftmost column in Figure 5) were also fatigue tested in the custom rig. Force-displacement loops and hysteresis widths for both samples are shown in Figure 6. In this initial test, the samples were subjected to a 20 N load amplitude at 10 Hz frequency for 1.8 Mcycles. Here, both samples survived the fatigue test without full fracture, but the hysteresis width of the 1050-3003 sample was noticeably larger than that of the 6101-3003 sample, which likely has to do with the larger thickness of the 6101 coupons (1.5 mm vs. 1.2 mm).

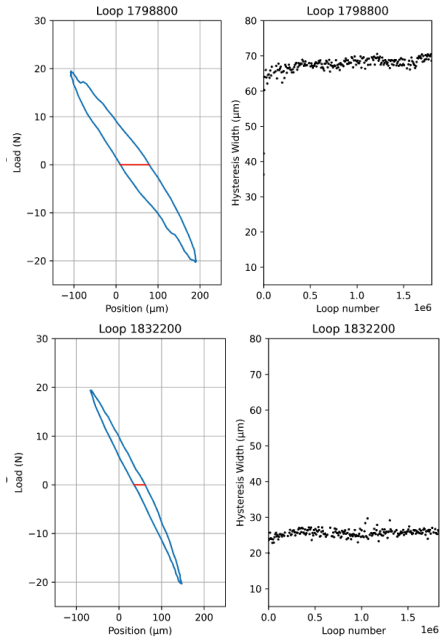

Figure 6 Force-displacement hysteresis loops and width of the hysteresis loops for the 1050-3003 (left) and 6101-3003 (right) material combinations. Both samples were laser welded with Brightline.

With these initial tests, the performance of the custom fatigue testing rig was evaluated, which revealed that 24/7 fatigue testing with simultaneous resistance measurement and auto-stop capability successfully were implemented. Additionally, temperature change in a cross-specimen subjected to the full 500 A-DC could be reliably measured. After this successful initial test of the custom rig, the different cases of the main investigation were then evaluated.

Case 1a – Effect of different weld shapes (Northvolt)

Since this is the first chronological case that was examined in this project, much of the focus in these first experiments centred around how and what types of analysis should be performed on these types of welded cross-specimens as well as what different types of fatigue damage can arise due to the different weld shapes (O (circle), S, L (to lines)).
Figure 7 compares the force-displacement loops of an S-shaped and an O-shaped weld subjected to different fatigue loads. The S-shaped weld experienced a 20 N load amplitude for 2 Mcycles followed by a 50 N load amplitude for up to 2 Mcyles. In Figure 7, only the

latter part of the test is shown. The hysteresis width of the S-shaped weld rose steadily throughout the duration of the second part of the fatigue test, reaching over 150 μm by 1.5 Mcycles. The S-shaped weld reached the auto-stop displacement threshold after approximately 1.56 Mcycles. The final force-displacement loop was seen to be irregularly shaped and elongated.

The O-shaped weld was subjected to a 20 N load amplitude for up to 2 Mcycles. The hysteresis width of the O-shaped weld remained relatively stable throughout the entire duration of the fatigue test, and the shape of the final force-displacement loop closely resembled that of the initial force-displacement loops.

LOM evaluation (Figure 8) of the S-shaped weld after fatigue testing showed the presence of two major fatigue cracks. One crack appears to have initiated on the surface of the 1050 tab away from the weld and then propagated along the laser weld fusion line before changing direction away from the weld, where the crack then appears to end at the sheet interface. The EBSD inverse pole figure (IPF) of the same weld shows clearly that the crack lies in the base material at the surface, and propagates along the heat affected zone (HAZ) and slightly inside the fusion zone. The other fatigue crack appeared to initiate at the junction between the weld fusion line and the sheet interface, where the crack then propagated and branched into the fusion zone. The longest branch of this crack propagated along the fusion line and just into the HAZ on the 3003 side (root side).

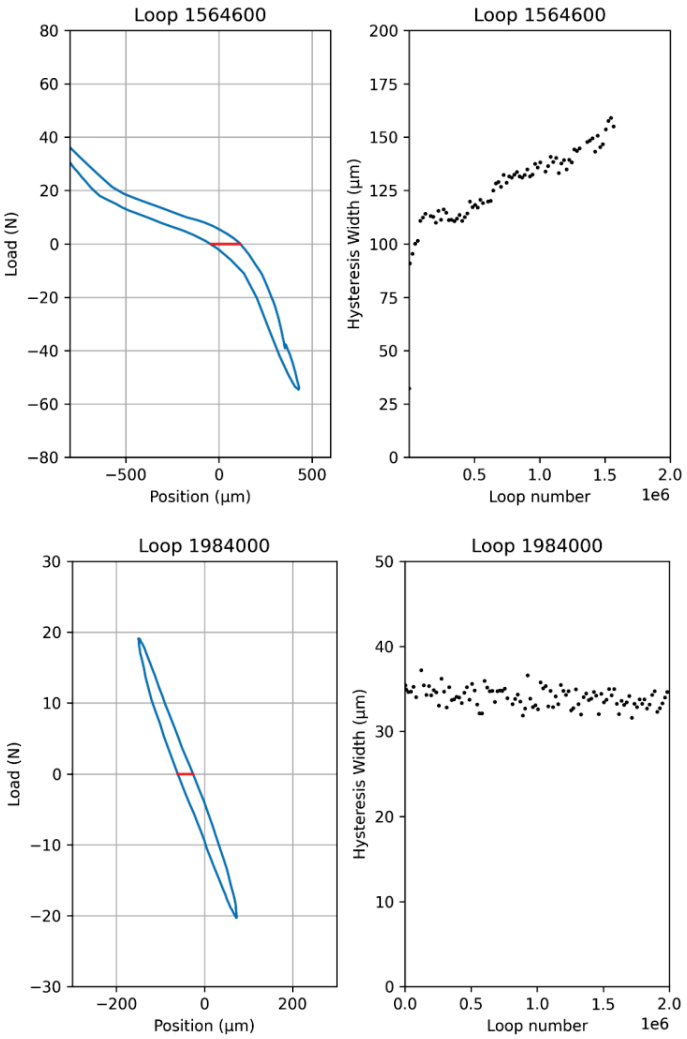

Figure 7 Force-displacement loops and hysteresis width for an S-shaped weld (top) and an O-shaped weld (bottom).

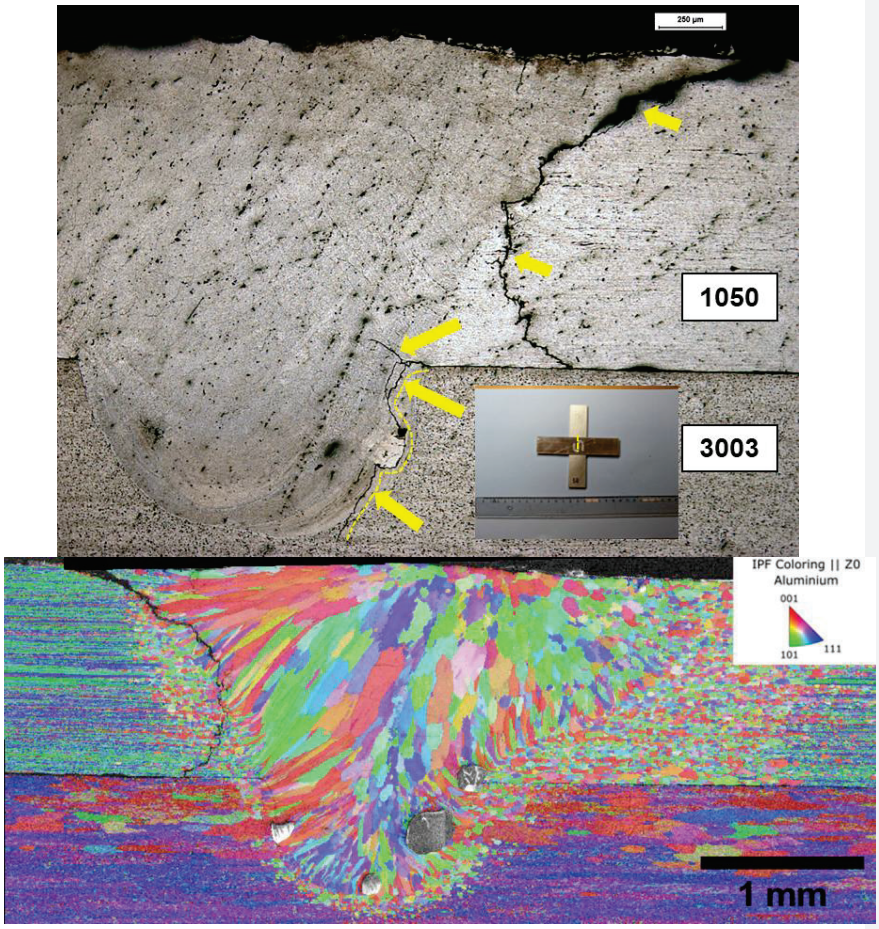

Figure 8 LOM image of a cross-section taken from the S-shaped weld after fatigue testing (top). Two main fatigue cracks are outlined with arrows. EBSD IPF of the same cross-section (bottom). Note that the images are mirrored.

In the O-shaped weld, a fatigue crack also initiating from the junction between the fusion line and sheet interface can be observed propagating primarily along the fusion line in Figure 9.

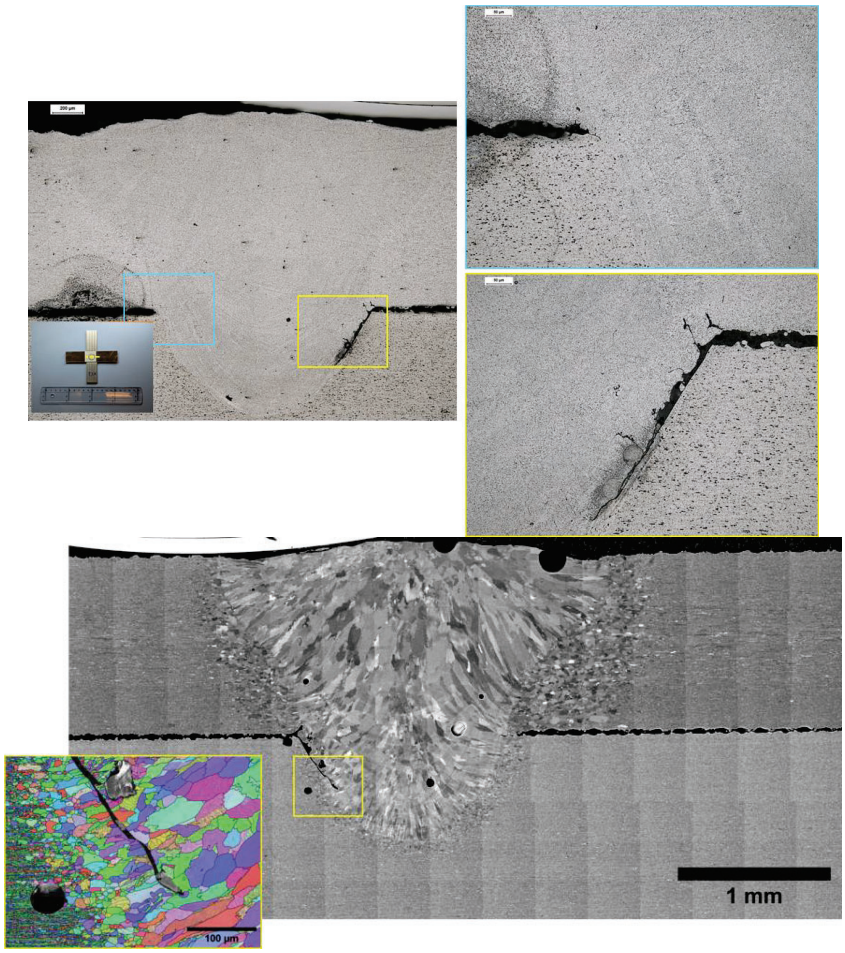

Figure 9 LOM image of a cross-section taken from the O-shaped weld after fatige testing (top left) with two higher magnification images showing the junction between the fusion line and the interface between the two sheets (top right). Forwardscattered (FSD) SEM image of the same weld (bottom) and EBSD IPF showing the crack tip (bottom left).

The first tests with applied high current (300 A) during fatigue testing (50 N, 2 Mcycles) were done using an S-shaped weld from this set of weld specimens. The force-displacement data, voltage drop, and temperature during fatigue testing for this specimen can be seen in Figure 10. Here, the hysteresis width rose steadily but at a much lower rate compared to the S-shaped weld tested without high current. However, this is likely due to a surface defect on the low-current sample which led to the formation of the severe fatigue crack at the 1050 tab surface. Otherwise, the fatigue crack initiated at a similar location and followed a similar path along the fusion line/HAZ in the high-current sample compared to the low-current sample, although the fatigue crack in the high-current sample propagated further into the 3003 busbar.

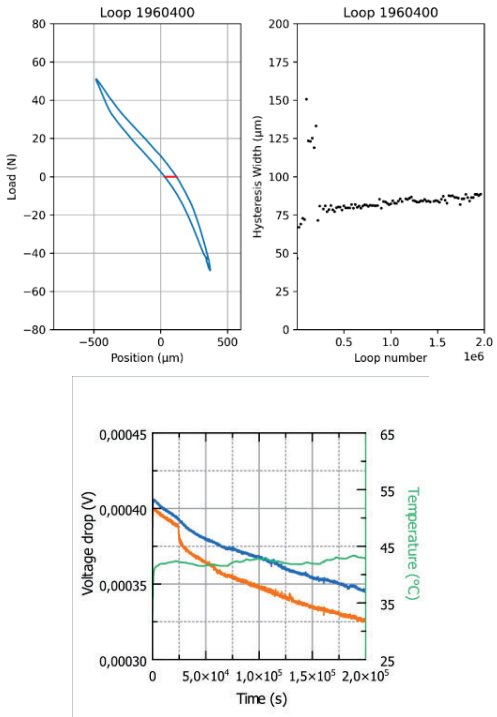

Figure 10 Force-displacement and hysteresis widths of an S-shaped weld subjected to fatigue under 300 A-DC (left). Voltage drop and temperature as measured by a thermocouple during fatigue testing (right).

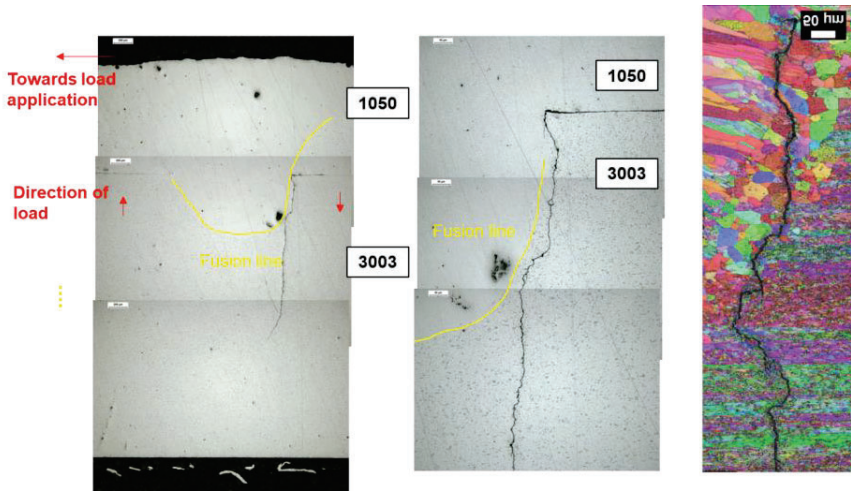

Figure 11 LOM micrographs showing the presence of a fatigue crack in the high-current S-shaped weld specimen (left and middle) and an EBSD IPF showing the crack propagation path (right).

Case 1b – Effect of different Al alloys (Lasertech)

Cross-sections of the as-received samples using different Al alloys as the tab material are shown in Figure 12 and Figure 13. In the 1xxx tab specimens, some porosity was observed, particularly in the weld root. In the initial trials, the 6101 tab specimens appeared to have insufficient penetration in the 3003 busbar (middle row of Figure 12), where some porosity can also be observed on either side of the weld where the fusion line meets the sheet interface. Therefore, new 6101 specimens were welded with higher heat input laser welding parameters. These parameters led to increased penetration (bottom row of Figure 12).

Medium power, medium scanning speed

Medium power, medium scanning speed

High power, low scanning speed

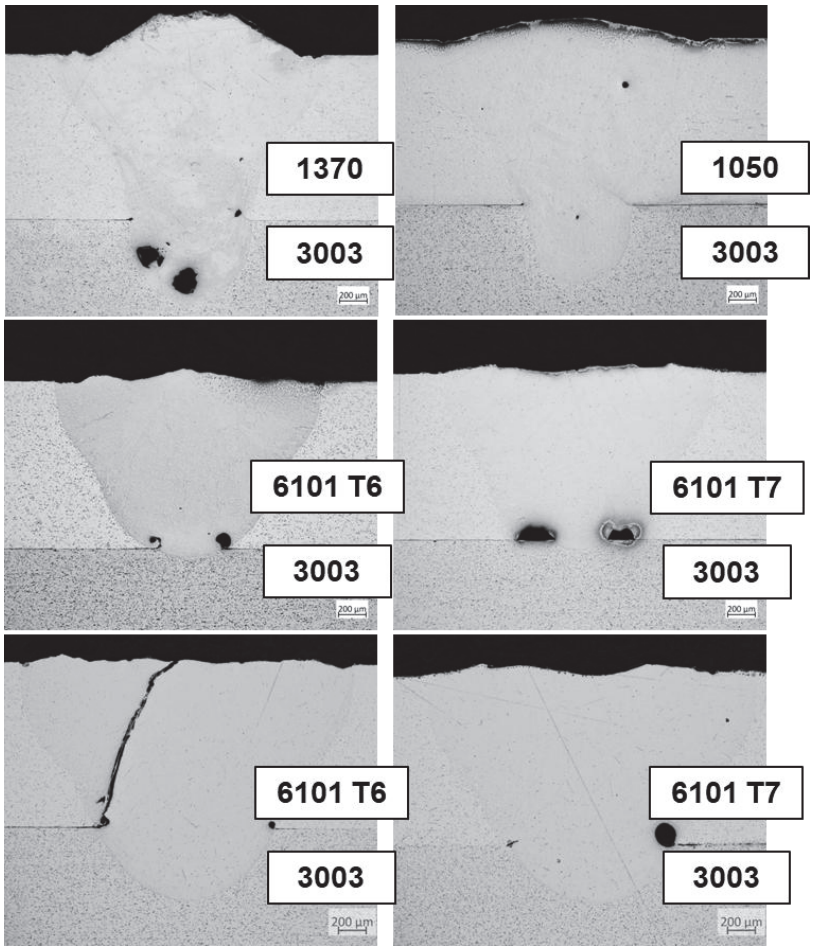

Figure 12 LOM micrographs of transverse cross-sections taken from the as-welded Lasertech samples.

The insufficient penetration of the 6101 specimens can also be seen in the longitudinal cross-sections in Figure 13. Although lack of penetration is also seen in the 6101 T6 specimen welding using the higher heat input laser welding parameters, this is thought to be the result of the longitudinal cross-section being taken too far from the weld centreline. That is to say, better penetration is expected in the 6101 T6 specimen welded using the

higher heat input laser welding parameters. Varying extents of solidification cracking were also observed in the end crater for all 6101 specimens, whereas the end crater regions of the 1xxx samples were crack-free.

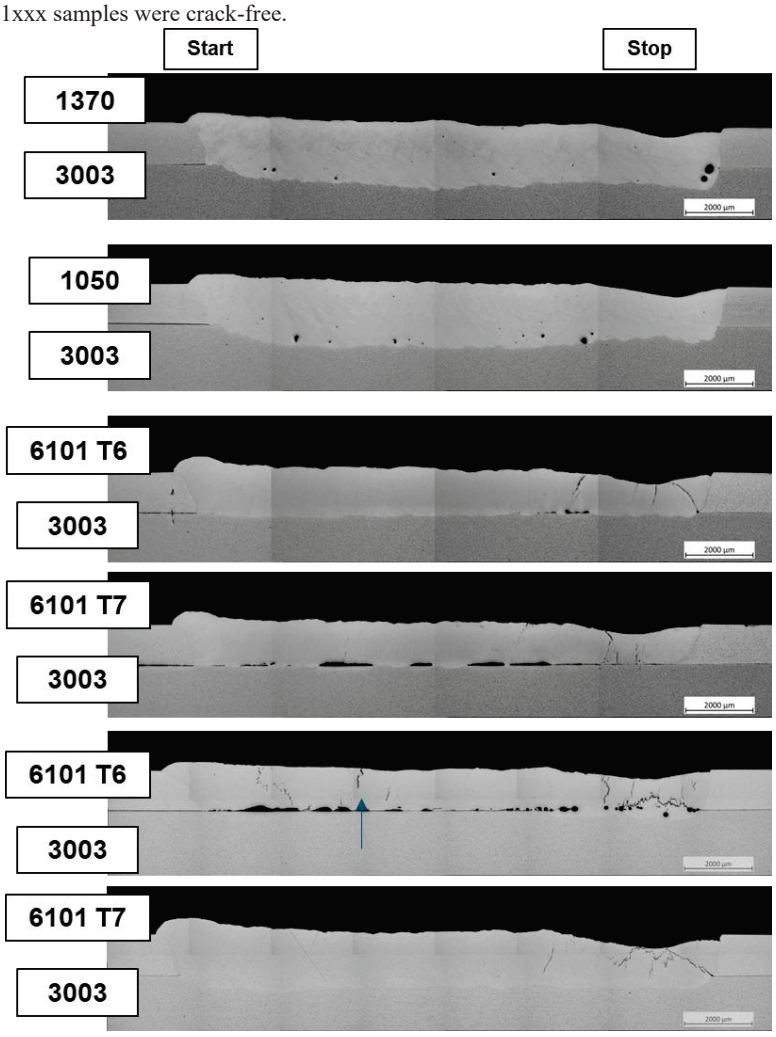

Figure 13 LOM micrographs of longitudinal cross-sect Medium power, medium scanning speed *Lasertech samples.*

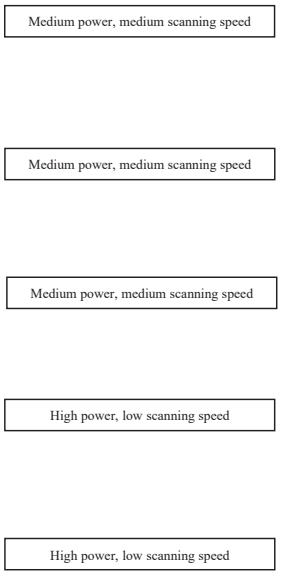

Force-displacement data during high-current (300 A-DC) fatigue testing for the 1370 and 1050 samples is shown in Figure 14. The total extension and hysteresis width of the 1370 tab sample was seen to rapidly rise, and the fatigue test was subsequently aborted via displacement auto-stop after only 160 kcycles. After removing the sample from the rig, it appeared that one of the two-line welds had fractured completely. The 1050 tab sample survived 2 Mcycles without triggering the displacement auto-stop, and the total extension and hysteresis width were relatively stable throughout the duration of the fatigue test.

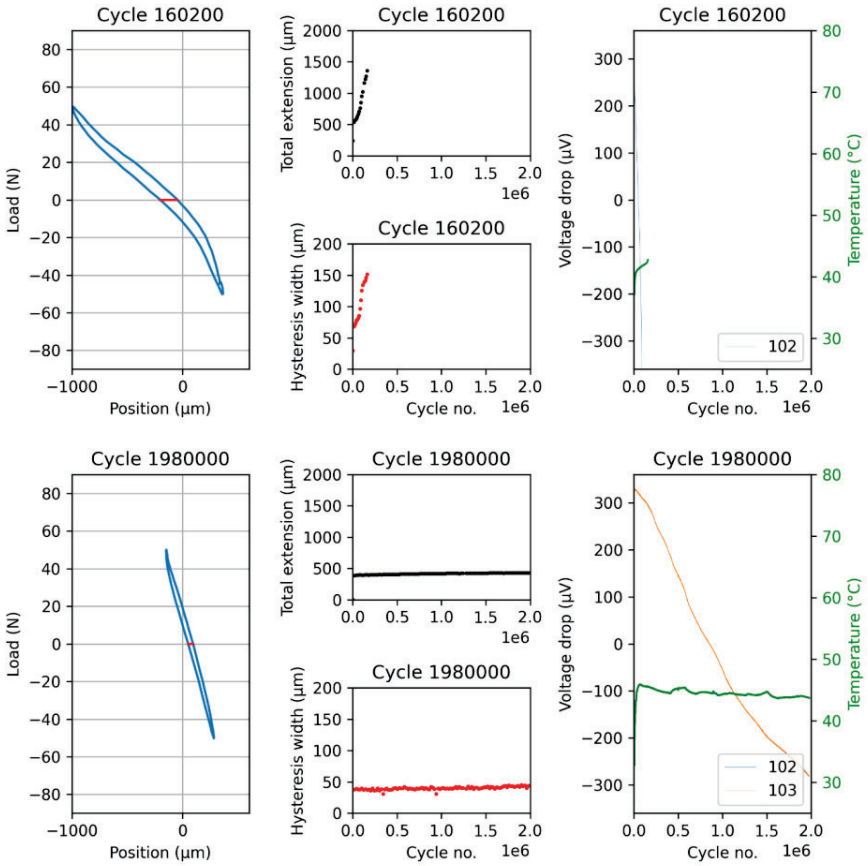

Figure 14 Force-displacement, voltage drop, and temperature for 1370 (top) and 1050 (bottom) samples subjected to 50 N load amplitude for 2 Mcycles under 300 A-DC applied current.

Similarly, both 6101 samples survived 2 M cycles without triggering the displacement auto-stop with relatively stable hysteresis loop characteristics. In both the 6101 and 1xxx samples, the steady-state temperature reached due to the application of 300 A-DC was between 40 °C – 45 °C.

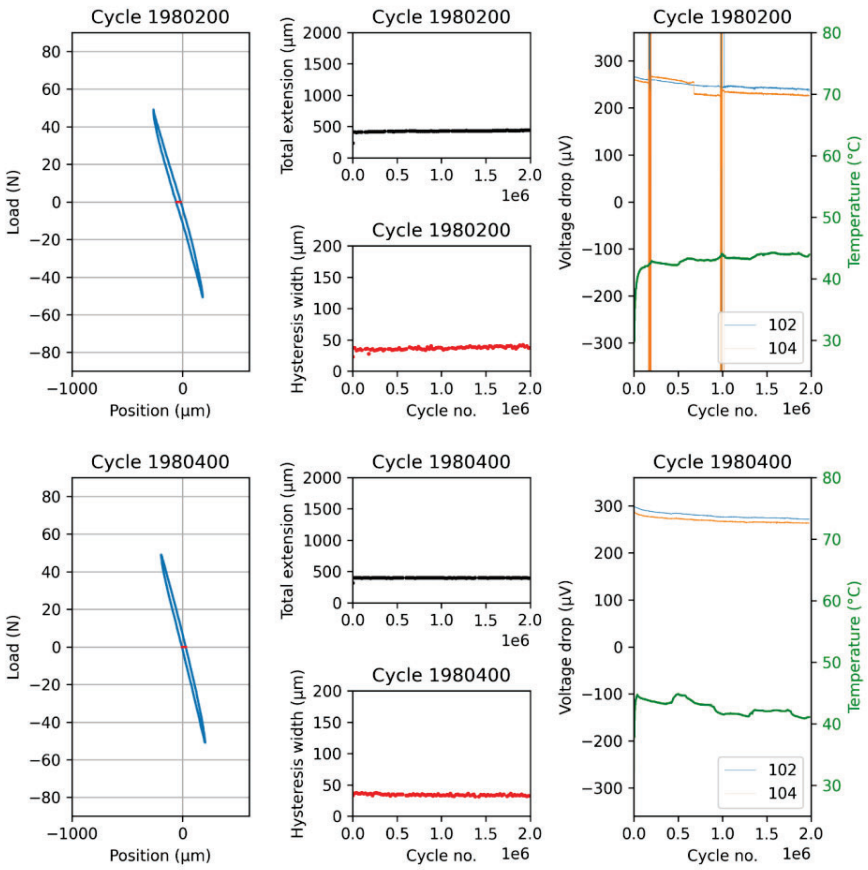

Figure 15 Force-displacement, voltage drop, and temperature for 6101 T6 (top) and 6101 T7 (bottom) samples subjected to 50 N load amplitude for 2 Mcycles under 300 A-DC applied current. Only the 6101 samples welded with high laser power and low scanning speed were fatigue tested.

Cross-sections of each sample after fatigue testing are shown in Figure 16. Significant fatigue damage was observed in the case of the 1370-3003 sample, where the right weld fractured completely through the weld metal, and a fatigue crack with substantial opening was found to be developing in the left. The 1050-3003 and 6101 T7-3003 samples did not possess any features of interest other than some gas porosity at the edge of the weld in the sheet interface. The 6101-T6 sample possessed what is likely a solidification crack in the right weld.

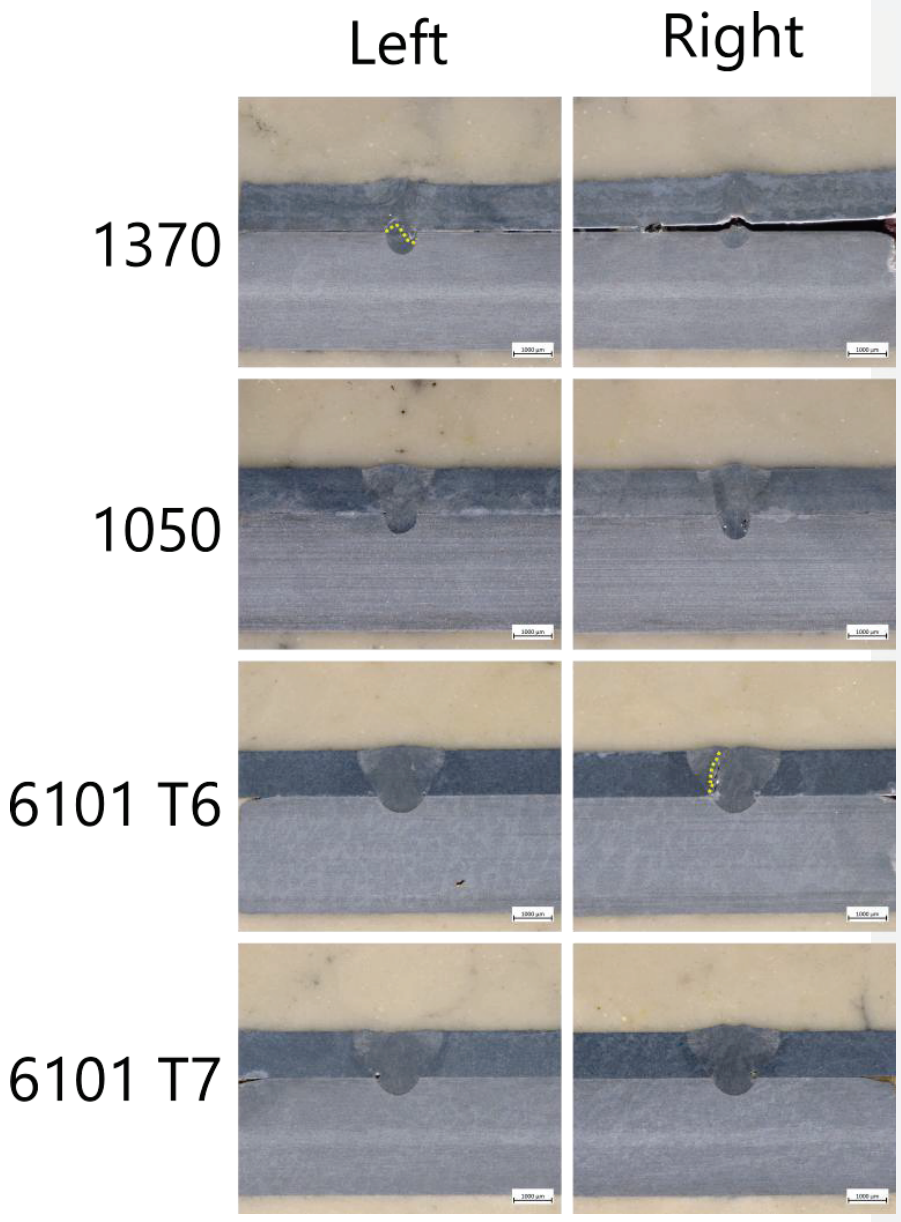
Left
Right
1370
1050
6101 T6
6101 T7

Figure 16 Cross-section macrographs of the 1050, 1370, 6101 T6 and 6101 T7 samples after fatigue testing for 2 Mcycle at 50 N load amplitude.

Case 1c – Effect of weld width at the sheet interface (Scania)

To determine the effect of different weld widths at the sheet interface on the fatigue performance of 1050-3003 cross-samples, welds were made with the same laser power (3800 W) as those welds made for the following case but with varying laser scanning speed. A low scanning speed was used to produce a nominal 1.4 mm weld width, and a high scanning speed was used to produce a nominal 0.7 mm weld width. Photographs of two representative samples are shown in Figure 17.

Figure 17 Photographs of the 1.4 mm weld width sample (left) and the 0.7 mm weld width sample (right).

These samples were subjected to 2 Mcycle, 50 N load amplitude under an applied 300 A-DC current. Load-displacement curves during fatigue testing can be seen in Figure 18. Although some asymmetry in the load-displacement loop was observed by the end of the fatigue test, the 1.4 mm weld width sample exhibited a stable hysteresis width with a somewhat increasing total extension during the 2 Mcycle. Given the increasing voltage drop, some fatigue damage was expected. The 0.7 mm weld width sample, however, gave a starkly degraded fatigue performance, triggering the autostop after only approximately 500 kcycle.

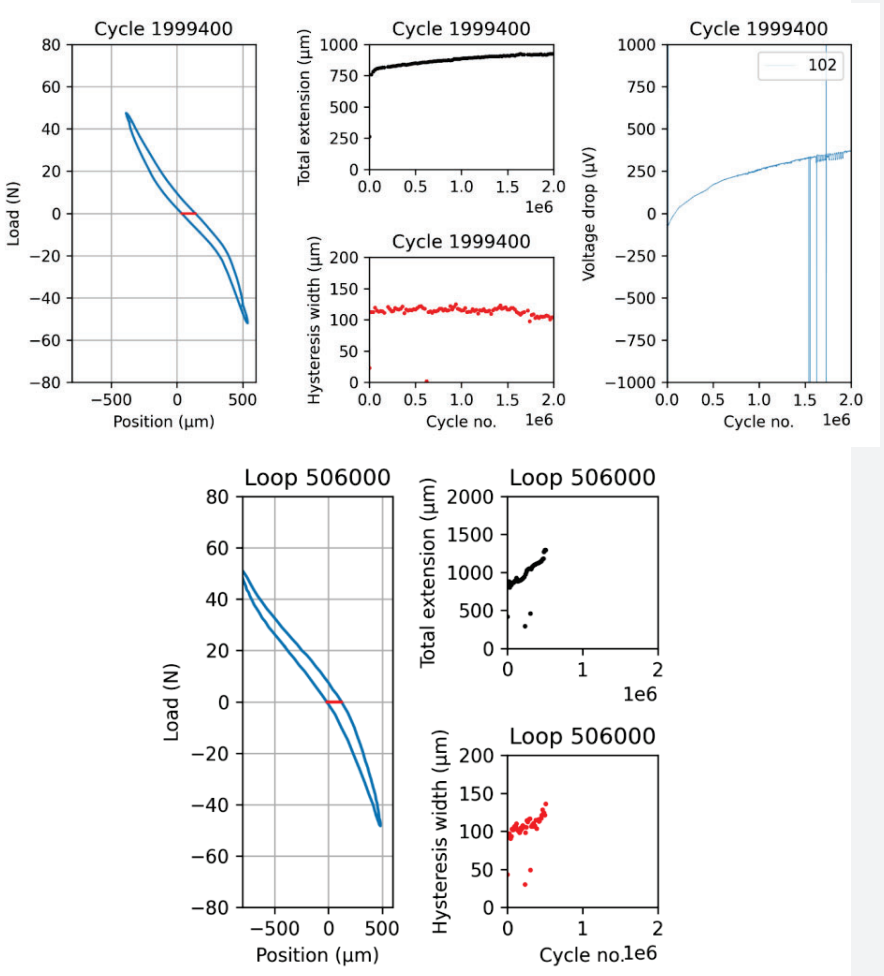

Figure 18 Load-displacment curves for the 1.4 mm weld width sample (top) and the 0.7 mm weld width sample (bottom). Voltage drop measurement was not available for the 0.7 mm weld width sample due to the fatigue test needing to be restarted several times.

To further investigate the presence of potential fatigue damage, CT scanning was performed on the fatigue-tested samples. The CT scans were used to measure the actual value of the weld width, which for the nominal 1.4 mm and 0.7 mm weld widths were found to be 1.5 mm and 0.85 mm, respectively. Measurements on the reference 1 mm weld width samples gave an average weld width of 1.1 mm. The 1.4 mm weld width sample (Figure 19) showed moderate porosity along the weld toes and solidification cracks in the end craters of all three welds. Additionally, fatigue damage was identified along the outer edges of the outer two welds, particularly in the rightmost (last) weld.

The 0.7 mm weld width sample (Figure 20) showed evidence of near catastrophic failure, with near-full material separation along most of the weld length primarily in the outer two welds. The centre weld also exhibited fatigue damage. In the outer two welds, it can be seen from the transverse cross-sections that the fatigue cracks appear to follow the direction of the assumed columnar grains (roughly 45°-60°) before meeting in the centre of the fusion zone.

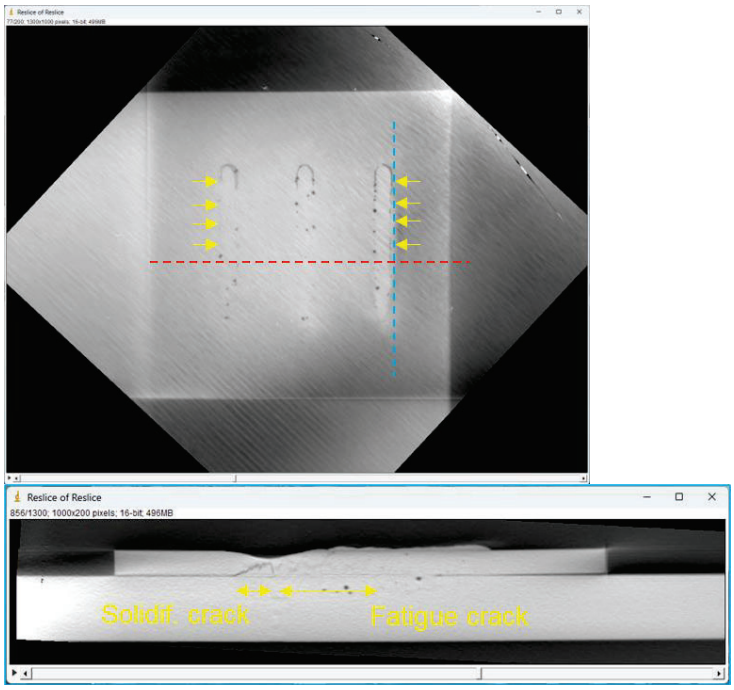

*Figure 19 CT cross-sections from the top (top), longitudinal (middle) and transversal (bottom) of the **1.4 mm weld width sample after fatigue (2 Mcycles, 50 N load amplitude)**.*

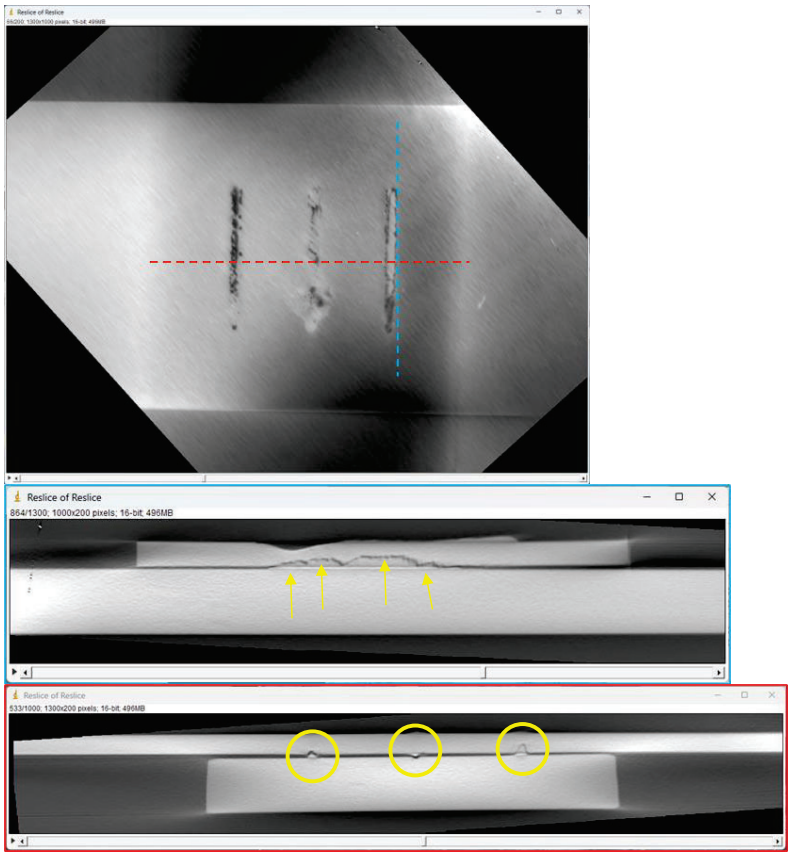

*Figure 20 CT cross-sections from the top (top), longitudinal (middle) and transversal (bottom) of the **0.7 mm weld width sample after fatigue (2 Mcycles, 50 N load amplitude)**.*

Another configuration tested in this case was a two-weld sample (as opposed to three-weld) using the same laser parameters that impart a 1 mm weld width. A photograph of a representative sample is shown in Figure 21. This sample was also subjected to cyclic loading for 2 Mcycle with a 50 N load amplitude under an applied 300 A-DC current. The resulting load-displacement data, temperature and voltage drop measurements are shown in Figure 22. Despite one fewer weld, this sample exhibited a rather stable total extension (less than 500 µm) and hysteresis width (less than 50 µm) during the entire fatigue test. In addition, a somewhat smaller increase in voltage drop (up to +250 µV) compared to the 1.4 mm weld width sample.

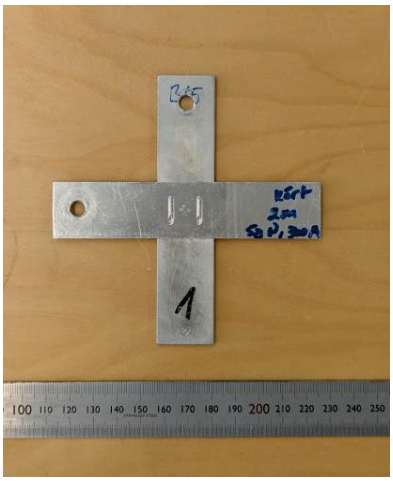

Figure 21 Photograph of the two-weld sample (1 mm weld width).

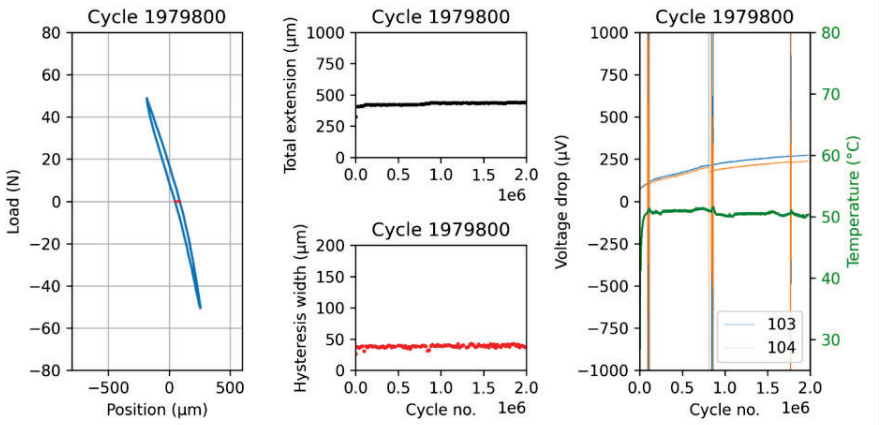

Figure 22 Load-displacement curves for the 1.4 mm weld width sample (top) and the 0.7 mm weld width sample (bottom). Voltage drop measurement was not available for the 0.7 mm weld width sample.

CT cross-sections of the two-weld 1 mm weld width sample after fatigue testing are shown in Figure 23. Moderate porosity was observed along the weld toes of both welds, and solidification cracking was also detected in both end craters. However, no obvious fatigue damage was identified in this sample.

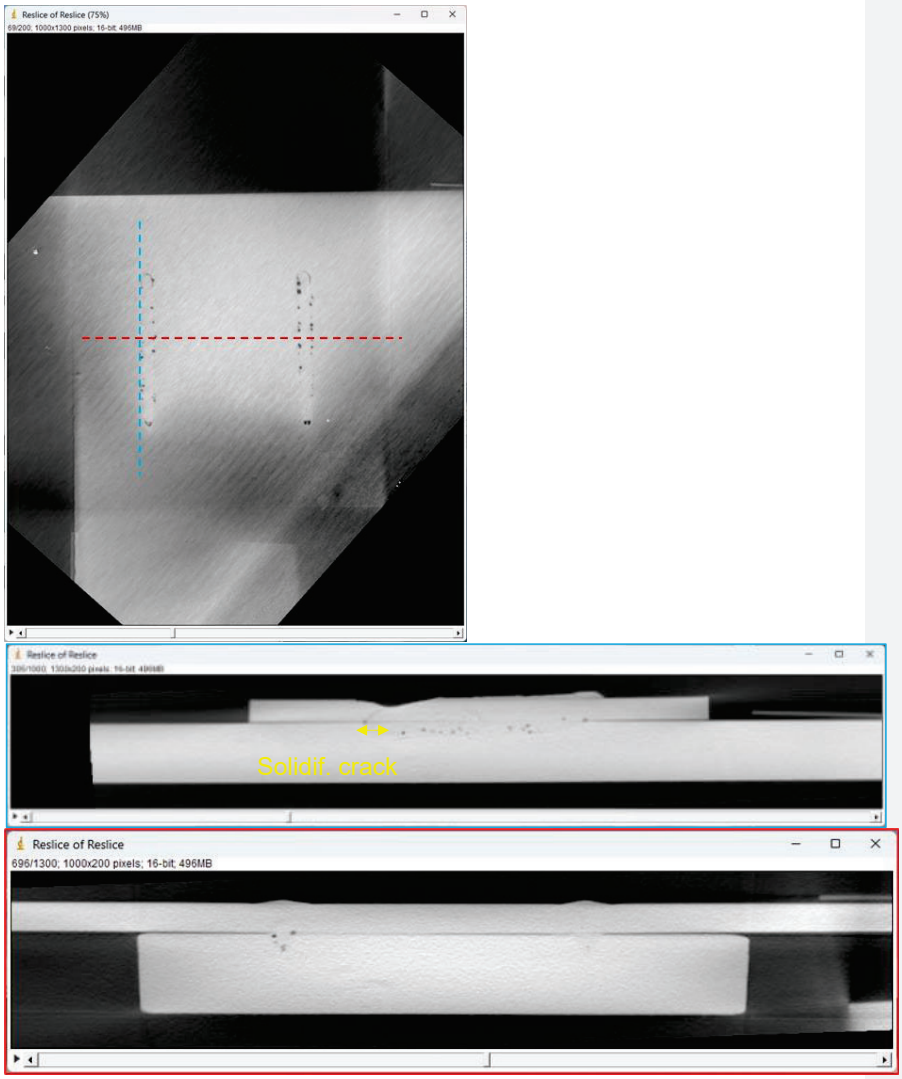

Figure 23 CT cross-sections from the top (top), longitudinal (middle) and transversal (bottom) of the two-weld 1 mm weld width sample after fatigue (2 Mcycles, 50 N load amplitude).

Case 1d – Effect of oxide thickness and annealing (Scania)

Photographs of samples representing the three different oxidation treatments (reference, room temperature RT, and elevated temperature OX) are shown in Figure 24.

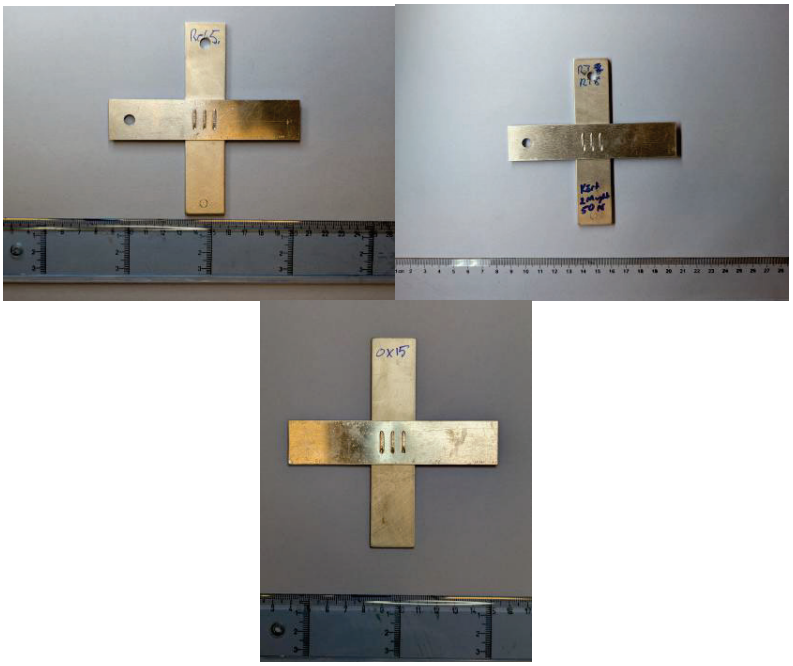

Figure 24 Photographs of representative samples of the reference condition, room-temperature oxidized (RT), and elevated temperature-oxidized (OX) laser-welded samples.

These samples were subjected to fatigue testing with 50 N load amplitude for 2 Mcycles. The load-displacement curves for each sample are given in Figure 25. In general, no significant differences in fatigue behaviour can be discerned from comparing the changes in total extension and hysteresis width. All three samples exhibit a very slightly increasing total extension and hysteresis width throughout the 2 Mcycles. Additionally, the voltage drop for all three samples was initially about -1 to -2 µV. Whereas the RT sample became only slightly less negative during the course of fatigue testing, the voltage drops in the ref. and OX samples eventually reversed polarity, increasing to +4 µV by the end of the fatigue test.

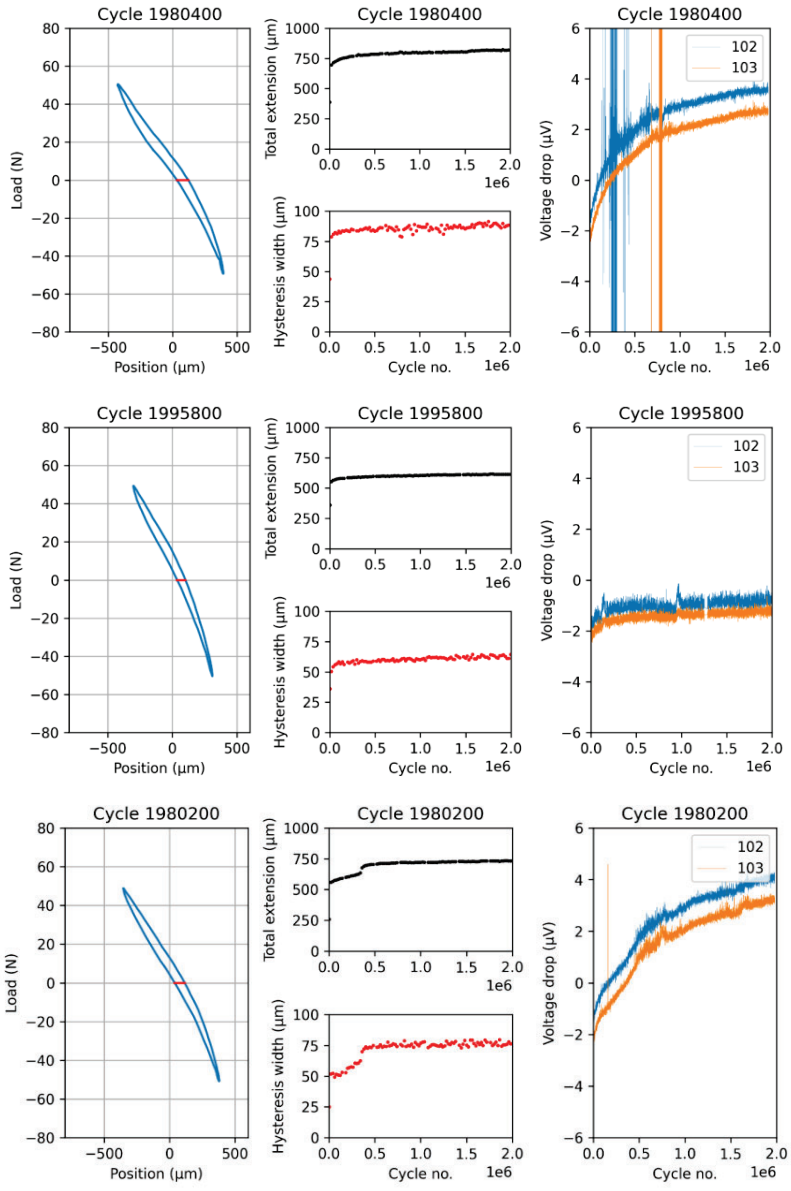
Cycle 1980400
Load (N)
Position (µm)
Cycle 1980400
Total extension (µm)
Hysteresis width (µm)
Cycle no.
1e6
Cycle 1980400
Voltage drop (µV)
102
103
Cycle no.
1e6
Cycle 1995800
Load (N)
Position (µm)
Cycle 1995800
Total extension (µm)
Hysteresis width (µm)
Cycle no.
1e6
Cycle 1995800
Voltage drop (µV)
102
103
Cycle no.
1e6
Cycle 1980200
Load (N)
Position (µm)
Cycle 1980200
Total extension (µm)
Hysteresis width (µm)
Cycle no.
1e6
Cycle 1980200
Voltage drop (µV)
102
103
Cycle no.
1e6

Figure 25 Load-displacement curves for a reference sample (top), RT sample (middle) and OX sample (bottom). 2 Mcycles, 50 N load amplitude. In addition to hysteresis width at zero load, the total extension from tip-to-tip is given. A measuring current of 3 A-DC was applied during testing.

To further investigate the effect of oxidation on weld quality aspects, such as the presence of porosity, and the subsequent impact on fatigue performance, CT scanning was performed on as-welded and fatigue-tested samples. Cross sections from three different directions are shown for each condition in Figure 26-Figure 31. One common feature across all sample conditions was the presence of solidification cracking in the end crater of all three welds on each specimen. This is likely due to an unoptimized weld stop imparting high cooling rates and therefore high shrinkage stresses acting on a typically columnar grain structure. In addition to solidification cracking, another common defect is gas porosity. Pores were typically found along the edges of the weld in the interface between the two aluminium strips as well as in the root of the weld. Interestingly, welds located in the centre of the joint area always exhibited less porosity than the outer welds. In general, the RT and OX-treated samples tended to exhibit more and/or larger pores at the sheet interface compared to the reference samples. These observations are further discussed in Section **Error! Reference source not found.**.

Clear signs of fatigue damage were observed in the reference and OX samples subjected to cyclic loading (Figure 27 and Figure 31), where fatigue cracks were seen to initiate from the existing solidification cracks in the end crater region and propagate along the outer weld edge on the outer two welds. Although solidification cracks were present in the end craters on all welds, including the centre weld, fatigue damage was not observed in any of the centre welds. Despite experiencing the same cyclic load as the reference and OX samples, no fatigue damage was identified in the RT sample. This observation may indicate that the qualitatively higher amount of porosity along the weld edge in the RT sample compared to the reference sample is less critical for fatigue performance than solidification cracking in the end crater or the notch-like effect of the sheet interface. The lack of fatigue damage may also explain the more stable voltage drop across the RT sample compared to the other two samples as seen in Figure 25.

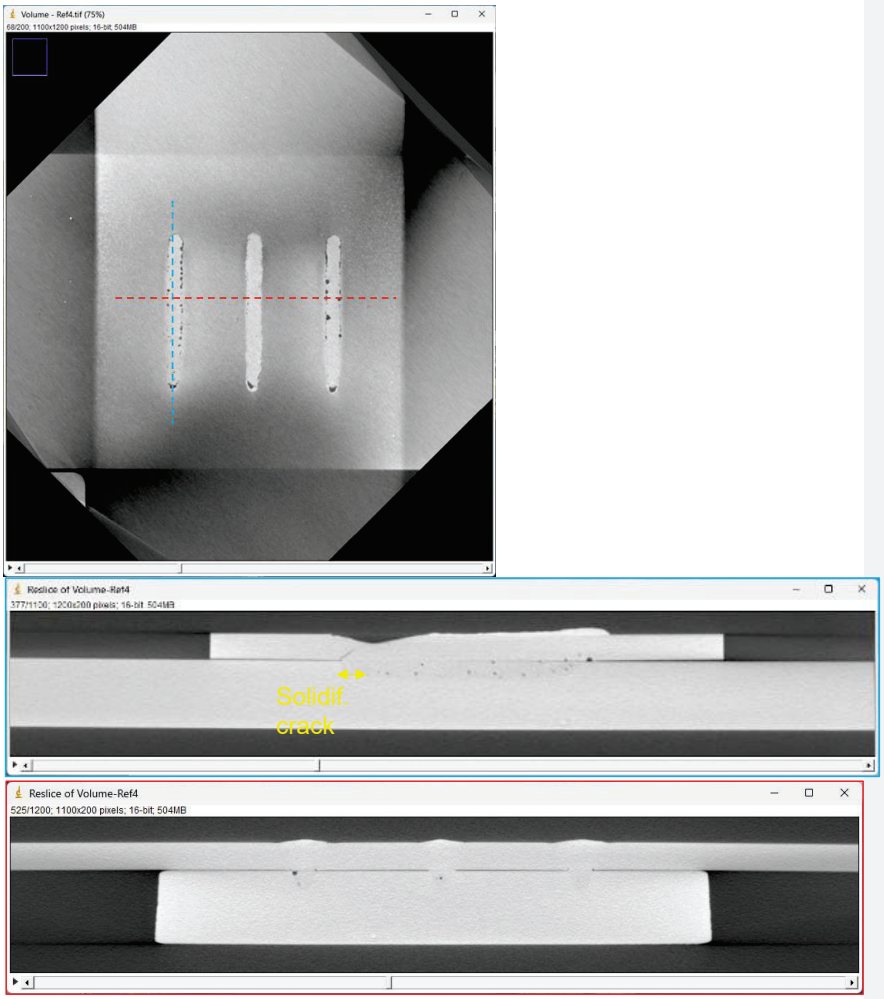

*Figure 26 CT cross-sections from the top (top), longitudinal (middle) and transversal (bottom) of the **reference 4 sample as-welded**.*

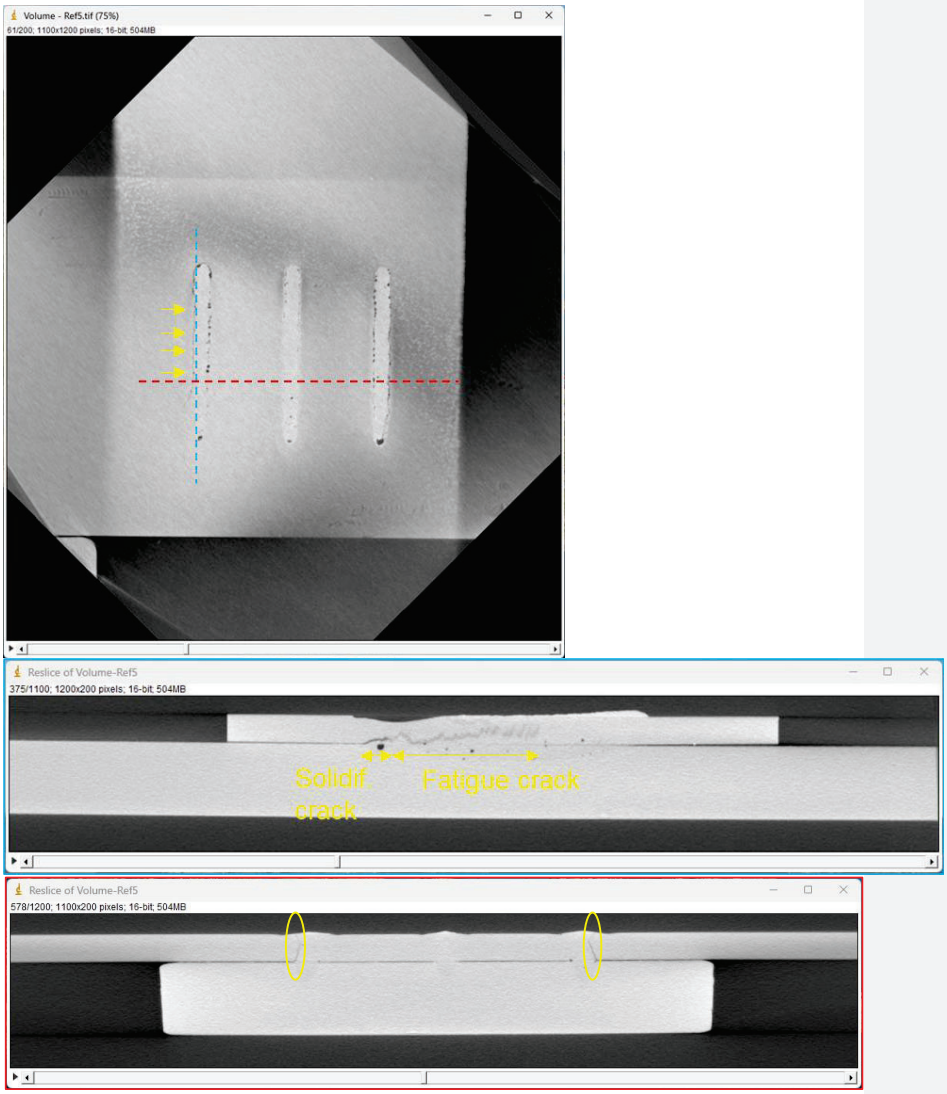

*Figure 27 CT cross-sections from the top (top), longitudinal (middle) and transversal (bottom) of the **reference 5 sample after fatigue (2 Mcycles, 50 N load amplitude)**.*

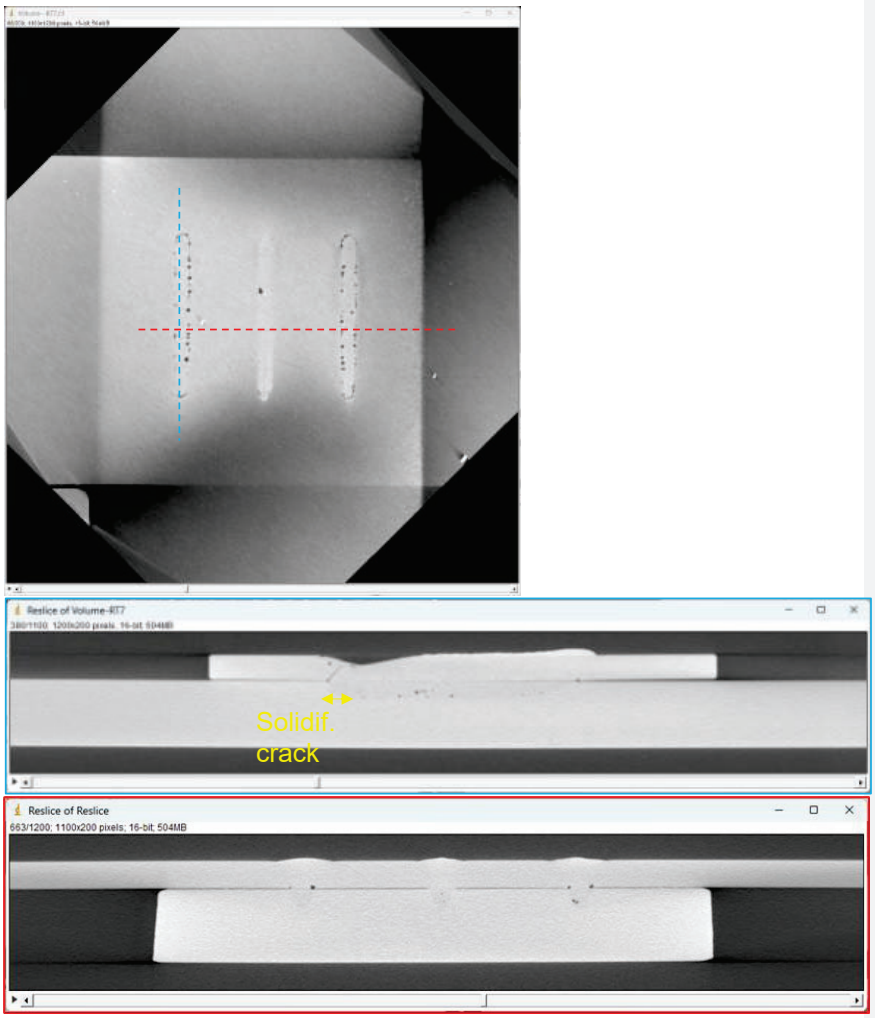

*Figure 28 CT cross-sections from the top (top), longitudinal (middle) and transversal (bottom) of the **RT7 sample as-welded.***

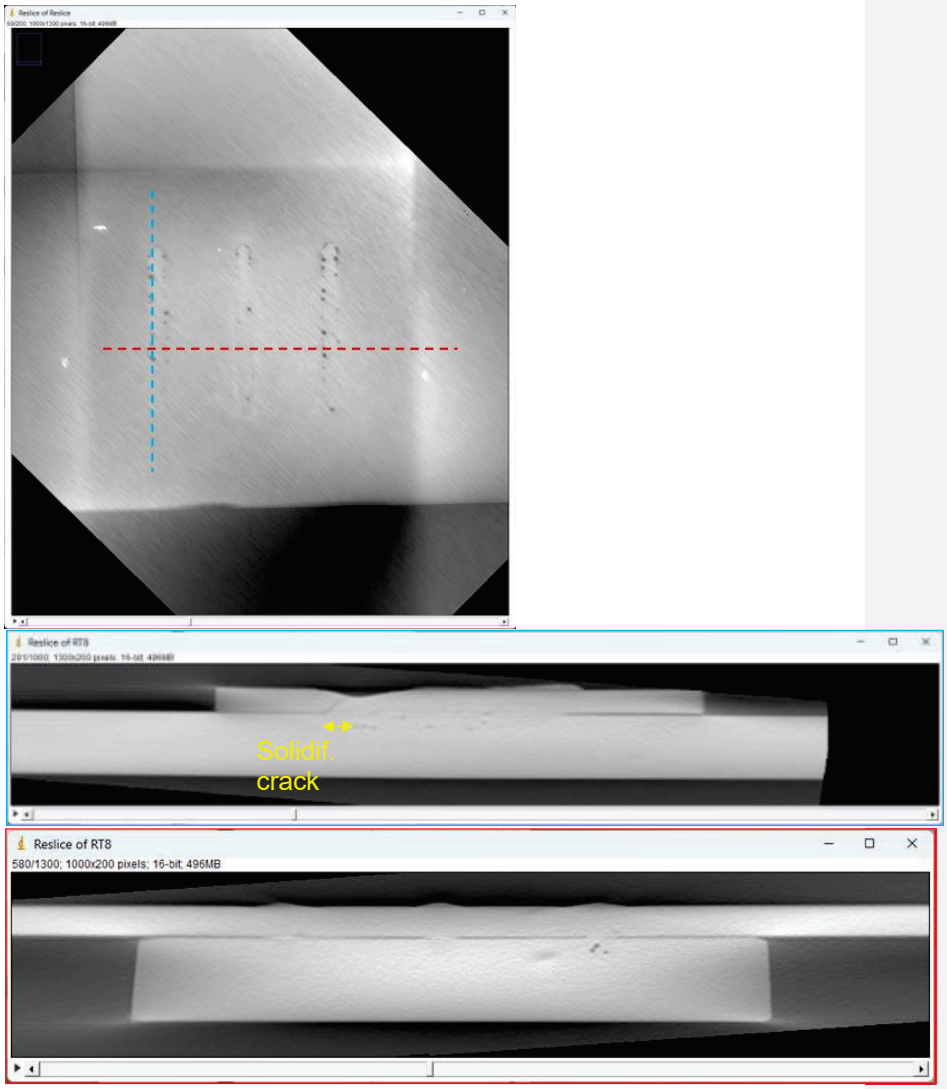

*Figure 29 CT cross-sections from the top (top), longitudinal (middle) and transversal (bottom) of the **RT8 sample after fatigue (2 Mcycles, 50 N load amplitude)**.*

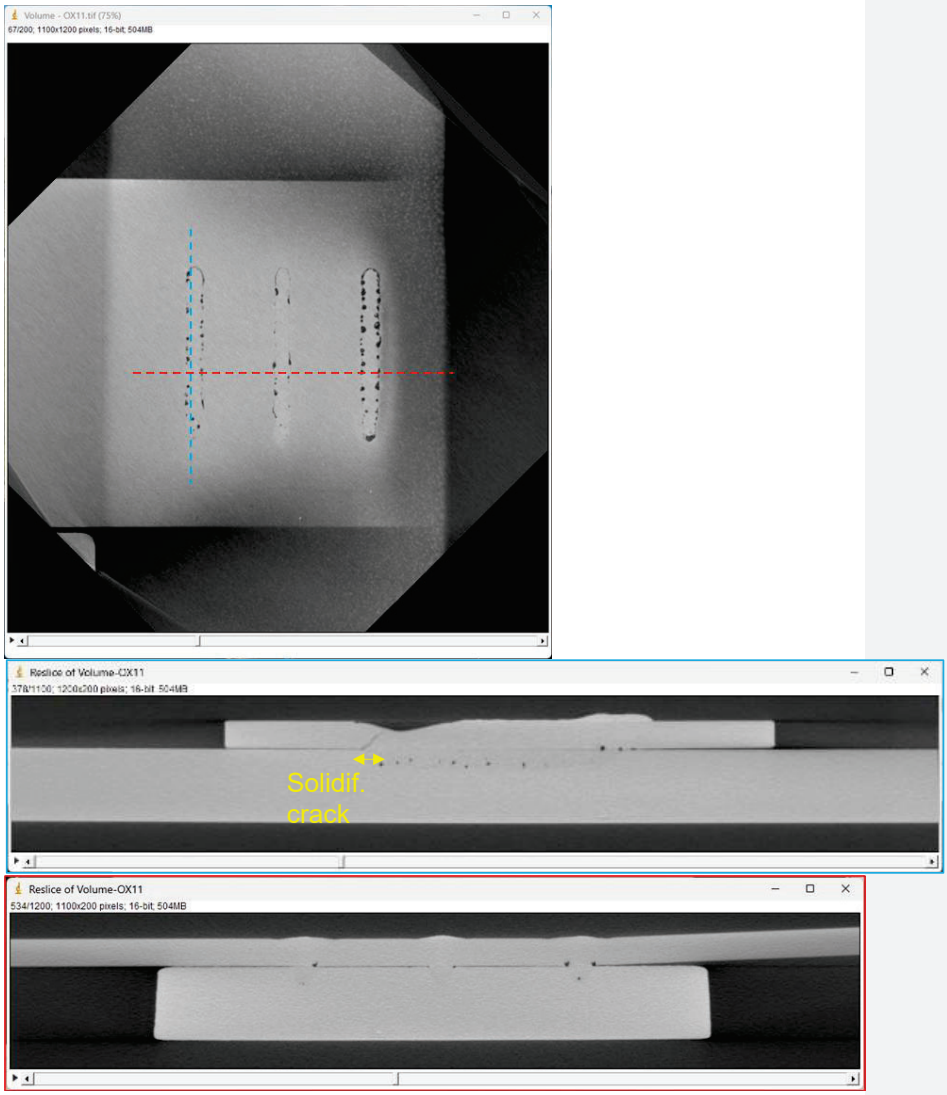

*Figure 30 CT cross-sections from the top (top), longitudinal (middle) and transversal (bottom) of the **OX11 sample as-welded**.*

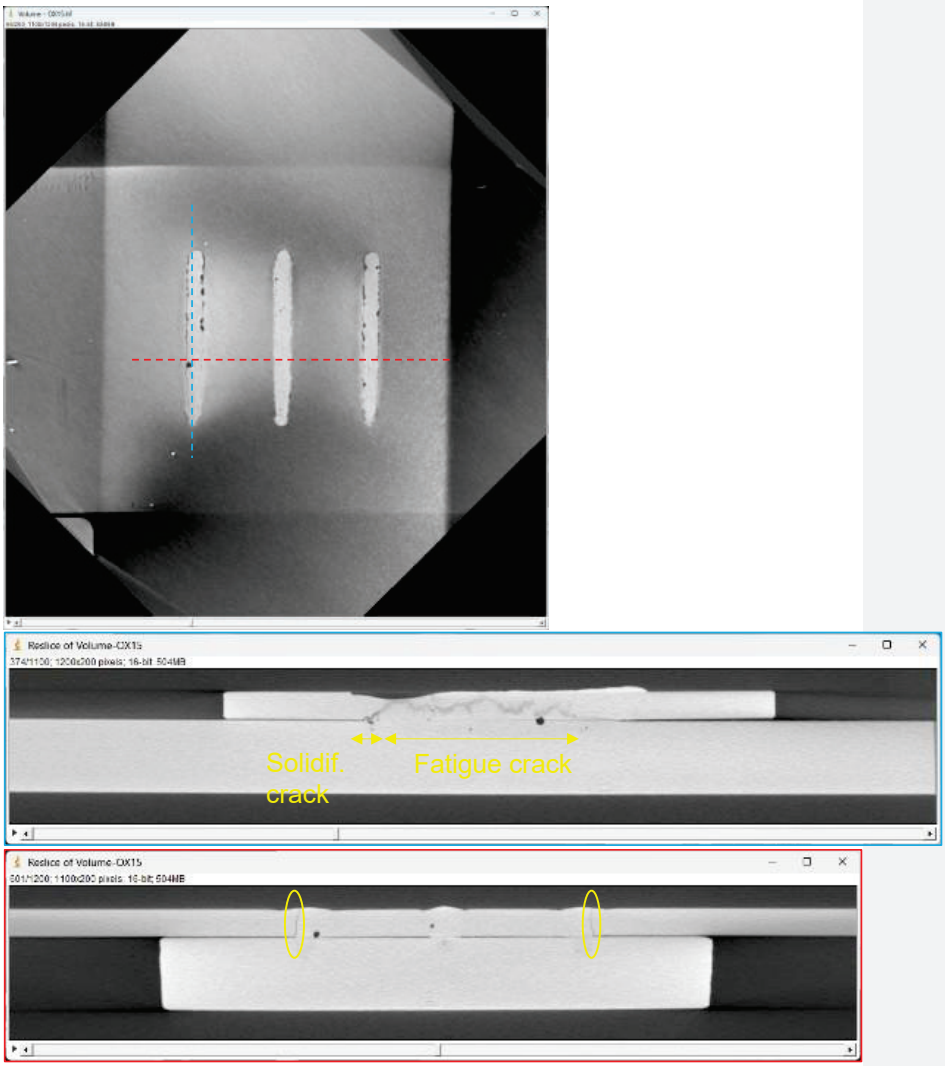

*Figure 31 CT cross-sections from the top (top), longitudinal (middle) and transversal (bottom) of the **OX15 sample after fatigue** (2 Mcycles, 50 N load amplitude).*

Another sample set tested in this case involved soft-annealing the 1050 aluminium “tab” before laser welding. The load-displacement curve during fatigue testing can be seen for the MJ17 sample in Figure 32. Although the sample survived the entire 2 Mcycle test without triggering the autostop, a steadily increasing total extension and hysteresis width can be observed throughout the fatigue test, likely indicating accumulation of fatigue damage. The voltage drop (disregarding the interruption at ~1.5 Mcycle) also tended to steadily increase over the course of testing.

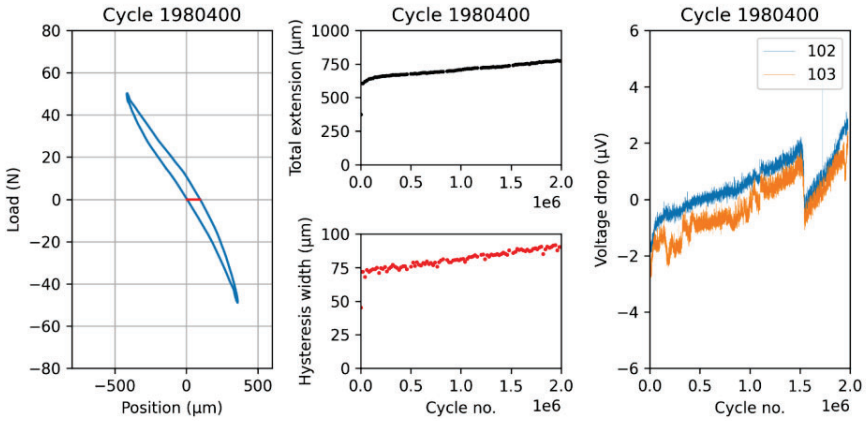

Figure 32 Load-displacement curves for the MJ17 soft-annealed sample. 2 Mcycles, 50 N load amplitude. In addition to hysteresis width at zero load, the total extension from tip-to-tip is given. A measuring current of 3 A-DC was applied during testing.

CT cross-sections for the as-welded MJ16 sample and the MJ17 after fatigue testing can be seen in Figure 33 and Figure 34. The as-welded sample exhibits noticeably less gas porosity along the weld toe compared to the reference and oxidized samples. However, solidification cracking was still present in the end crater of all three welds. After fatigue testing, fatigue cracking along the weld edges can be observed in Figure 34. In this case, the fatigue crack has even propagated through the base material. Although difficult to represent with 2D cross-sections, the fatigue damage within and near the fusion zone was found to be more extensive compared to the reference case. These likely causes behind these findings are discussed further in Section **Error! Reference source not found.**.

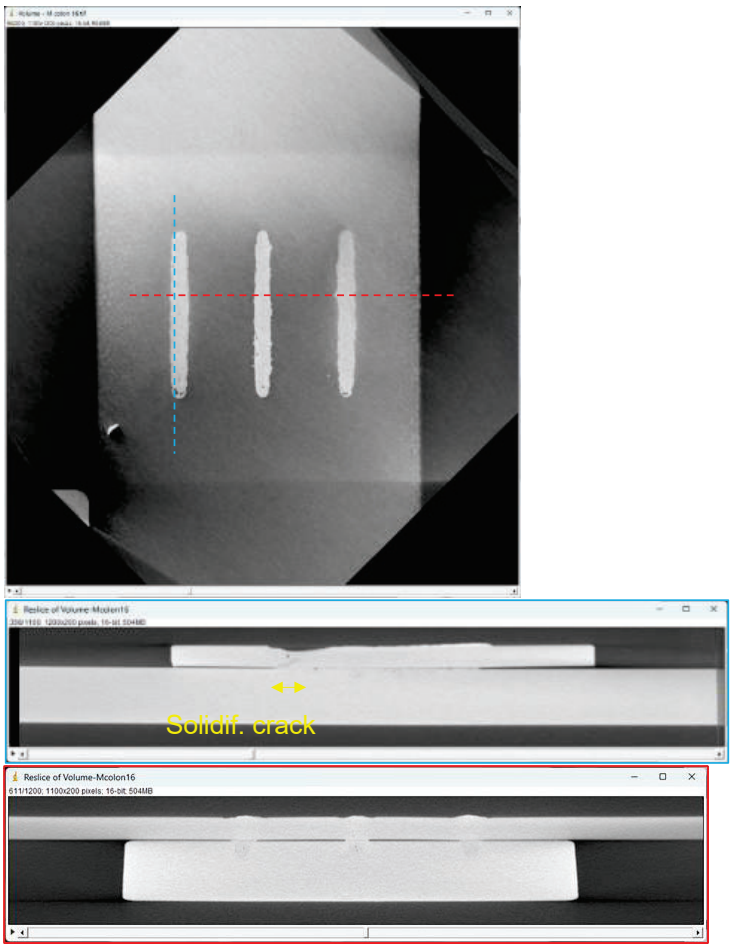

*Figure 33 CT cross-sections from the top (top), longitudinal (middle) and transversal (bottom) of the **MJ16 as-welded**.*

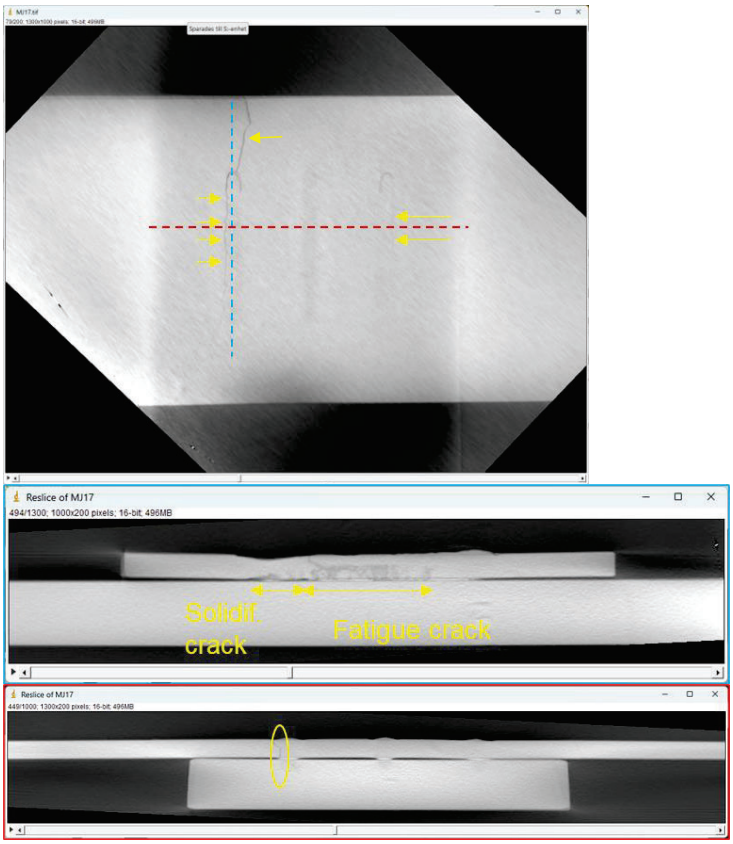

*Figure 34 CT cross-sections from the top (top), longitudinal (middle) and transversal (bottom) of the **MJ17 sample after fatigue** (2 Mcycles, 50 N load amplitude).*

Case 1e – Effect of heat treatment and connection with FEM simulation (Volvo Cars)

In this case, three different weld shapes, including a circular weld, were tested to examine the effect of the weld geometry on fatigue behavior. FEM simulation of the three different weld shapes was also performed at Volvo Cars in order to better understand the stresses acting on the weld. Only results from the circular weld are included in this public report.

First, a representative circular weld was characterized in the as-welded condition. A photograph of the sample can be seen in Figure 35. A cross-section (Figure 36) was taken along the yellow line in Figure 35 to characterize the as-welded condition. This cross-section shows a weld profile that has noticeably more penetration and a narrow weld root compared to the other laser welding cases in this work.

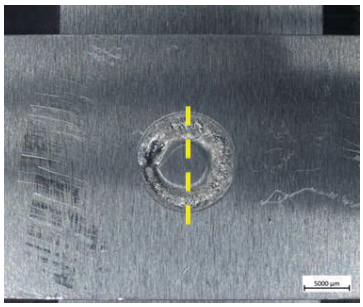

Figure 35 Macrophotograph of one of the circular weld samples. The yellow line indicates the orientation of the cross-section taken for further characterization.

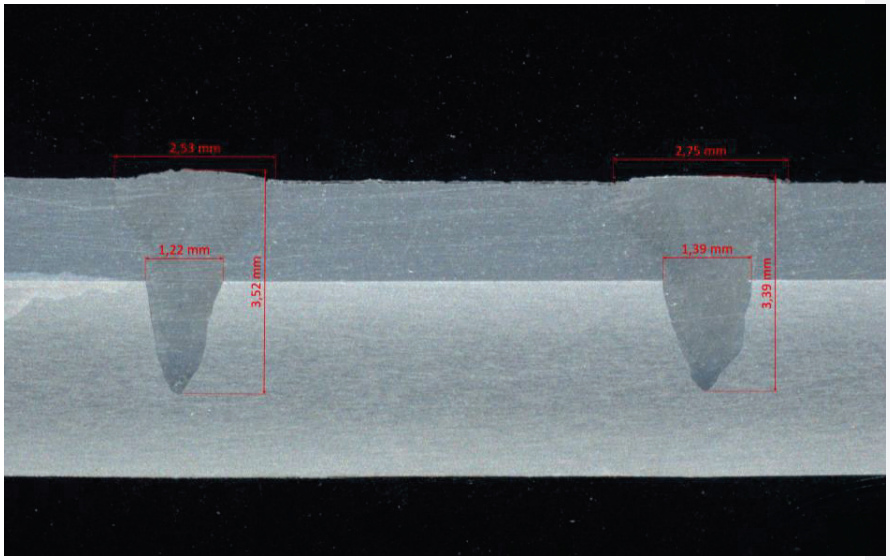

Figure 36 Macrograph cross-section of the circular weld with penetration and weld width measurements.

Vickers microhardness (HV0.05) measurements were taken in both the 1050 and 3003 base materials far away from the weld as well as in the top and bottom of the weld metal. An average of four measurements were used. Two hardness profiles were also extracted from inside the weld metal out into the base material. These measurements are shown in Figure 37. The Vickers microhardness measurements revealed a similar hardness (33.2 HV0.05) between the 1050 base metal and the upper portion of the weld metal, likely indicating little mixing of Mn from the 3003 into the top part of the melt pool. The hardness profile taken from the top part of the weld into the 1050 base material showed a similar hardness along the entire profile. Contrarily, softening of the weld metal compared to the 3003 base metal (45.0 HV0.05 vs. 57.9 HV0.05) could be observed in the weld root. The hardness profile showed the great extent of softening in the weld metal near the fusion line, where a hardness of approximately 36 HV0.05 was measured. A narrow (<50 µm) heat affected zone (HAZ) is evident since the hardness was seen to rapidly increase outside of the weld metal continuing into the 3003 base material.

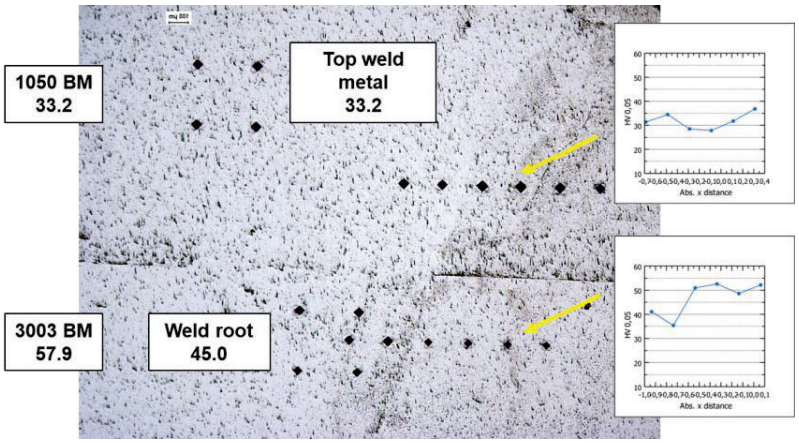

Figure 37 Micrograph of one side of the circular weld (left) with Vickers microhardness (HV0.05) data inset and hardness profiles taken from the fusion zone into the base metal.

For case 1e "A", circular weld samples were subjected to fatigue in two steps: first, 10 kcycles at 80 N load amplitude, followed by up to 10 Mcycles at 25 N load amplitude. The load-displacement curves for a representative sample are shown in Figure 38. In this case, it can be seen that the total extension and hysteresis width rise rapidly during the initial 10 000 cycles under the 80 N load amplitude. During the next stage of fatigue testing under 25 N load amplitude, however, both the total extension and hysteresis width remained quite stable.

After fatigue testing, these samples were cross-sectioned and investigated via LOM. A representative cross-section is shown in Figure 39. Here, fatigue damage was limited to rather short cracks which initiated at the junction between the fusion line and the sheet interface, and which then propagated into the weld metal. Given the stability of the hysteresis loop during the 25 N load amplitude stage, it seems reasonable to assume that the bulk of the observed fatigue damage occurred during the 80 N load amplitude stage.

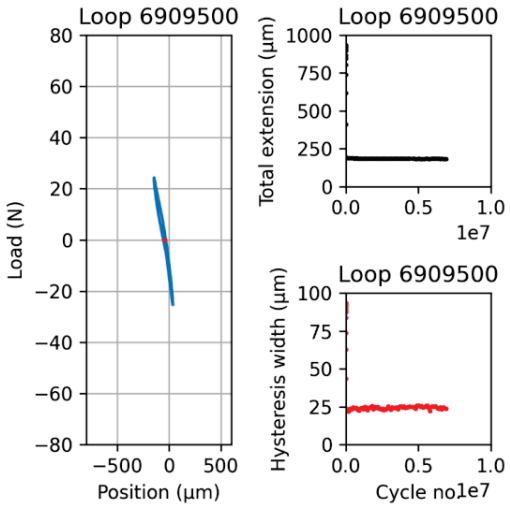

Figure 38 Load-displacement curves for a circular weld Volvo Cars sample. 10 kcycles at 80 N load amplitude followed by 7 Mcycles, 25 N load amplitude. In addition to hysteresis width at zero load, the total extension from tip-to-tip is given.

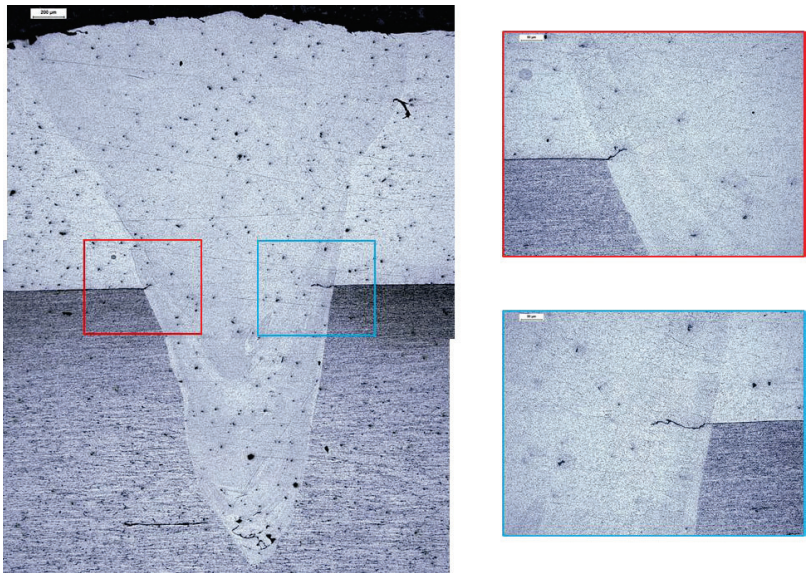

Figure 39 LOM micrograph of a circular weld cross-section ***after fatigue testing (10 kcycles at 80 N load amplitude followed by approximately 7 Mcycles at 20 N load amplitude)****.*

For case 1e “B”, samples were instead subjected to a constant 80 N load amplitude for up to 2 Mcycles. This fatigue testing was done with both as-welded samples and samples that had been heat-treated for one month at 120 °C to determine the effect of heat treatment on fatigue performance. To better understand the stresses on the sample that arise under this loading, finite element modelling (FEM) was performed by Volvo Cars using the same sample geometry and applied load. A schematic of the fatigue testing rig and weld sample as implemented in the FEM modelling software can be seen in Figure 40.

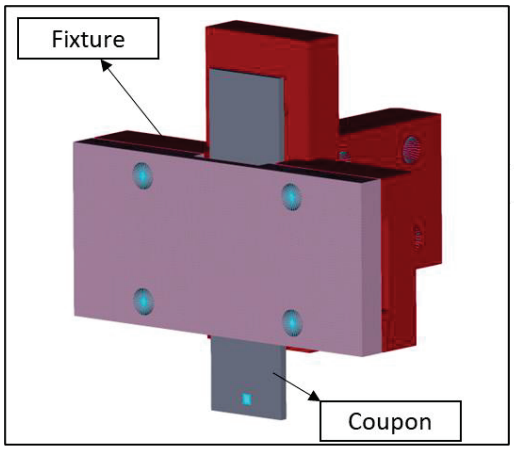

Figure 40 FEM model of the weld sample inside the fatigue testing rig.

Results from the FEM simulation are shown in Figure 41, where the von Mises stress and individual stress components arising in the sample are illustrated. The von Mises stress is a scalar quantity typically used to determine if a ductile material will yield under complex (3D) loading. The von Mises stress is given by:

$$\sigma_{\mathrm{v}} = \sqrt{\frac{1}{2}\left[(\sigma_{11}-\sigma_{22})^2+(\sigma_{22}-\sigma_{33})^2+(\sigma_{33}-\sigma_{11})^2\right]+3\left(\sigma_{12}^2+\sigma_{23}^2+\sigma_{31}^2\right)}$$

where the subscripts refer to the different normal stress components (11, 22, and 33) and the different shear stresses (12, 23, 31). The highest value of von Mises stress of 162.85 MPa was found occur at the bottom edge of the weld (closer to the point of load application) in the interface between the two aluminium pieces. Similarly, the maximum values of the x- and y-components of stress (169.5 MPa and 78.5 MPa, respectively), which are expected to be the most critical for fatigue crack propagation, were located at the bottom edge of the weld in the sheet interface. In general, stress appeared to be concentrated around the lower half of the circular weld.

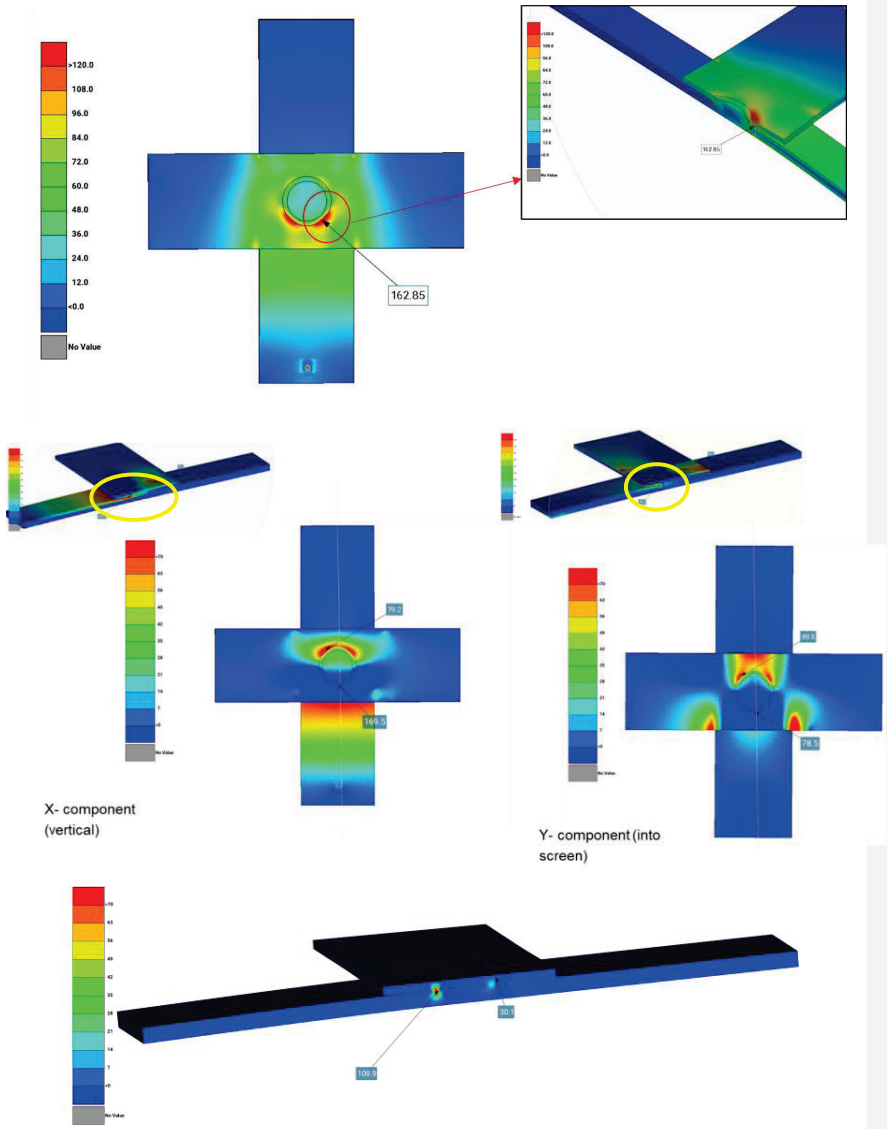

Figure 41 FEM results showing the von Mises stress (top), x-component (middle left), y-component (middle right), and z-component (bottom) of stress in the sample. Inset images show the distribution of each stress component along a cross-section.

Fatigue testing was conducted using an 80 N load amplitude over 2 Mcycles with a measuring current of 3 A-DC. Load-displacement data for the as-welded sample and the 1 month heat-treated sample are shown in Figure 42. Fatigue testing of both samples was interrupted by the triggering of the 700 µm autostop threshold. Both samples exhibited a rapid increase in both total extension and hysteresis width during testing. Similarly, the voltage drop in both samples rose significantly before the test was interrupted. The as-welded sample survived 820 kcycles before reaching the autostop threshold, whereas the one month heat-treated sample survived only 620 kcycles, which can be interpreted as worsened fatigue performance caused by the heat treatment.

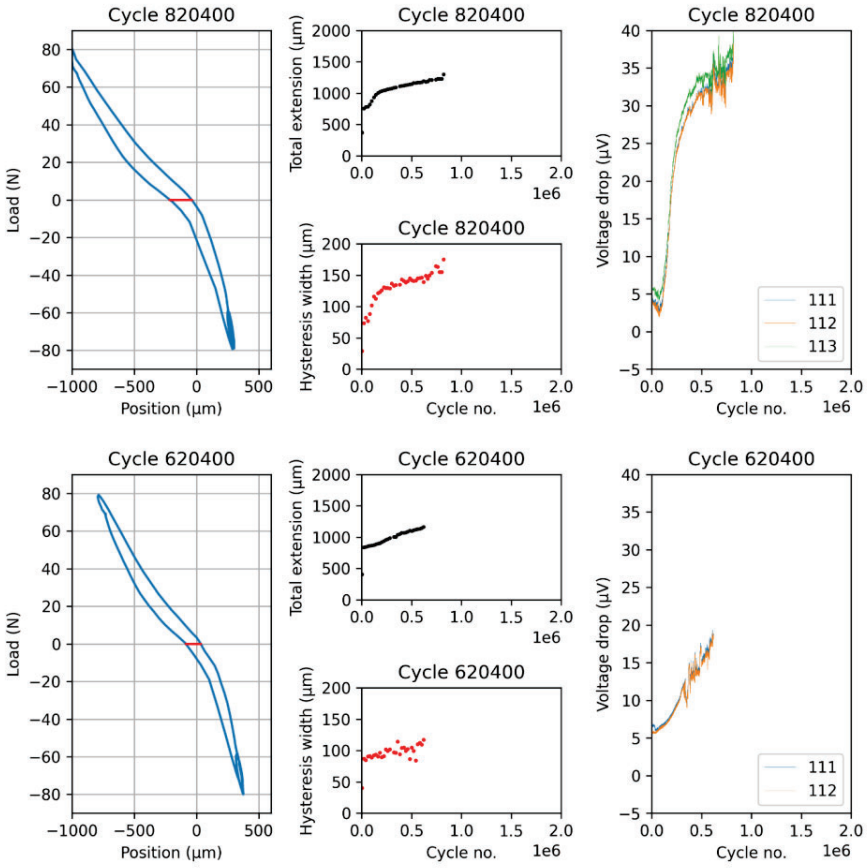

Figure 42 Load-displacement curves for circular weld Volvo Cars samples ***as-welded (top) and after one month heat-treatment at 120 °C (bottom)****. 2 Mcycles at 80 N load amplitude. In addition to hysteresis width at zero load, the total extension from tip-to-tip is given. A measuring current of 3 A-DC was applied during testing.*

CT cross-sections of the heat-treated sample after fatigue testing are shown in Figure 43 (the as-welded sample was still being tested when the last round of CT scanning was performed and is therefore not available). Significant fatigue damage accumulated in the lower half of the circular weld, which is in good agreement with the stress distribution predicted by the FEM simulation. The fatigue crack was also found to branch off into the 1050 base material on the right side of the weld (second image from top in Figure 43). In the transverse cross-sections, it was seen that the fatigue crack primarily propagates through the fusion from both sides of the junction of the fusion line with the sheet interface.

Additionally, thin fatigue cracks propagating vertically along the weld depth (blue image in Figure 43) were observed.

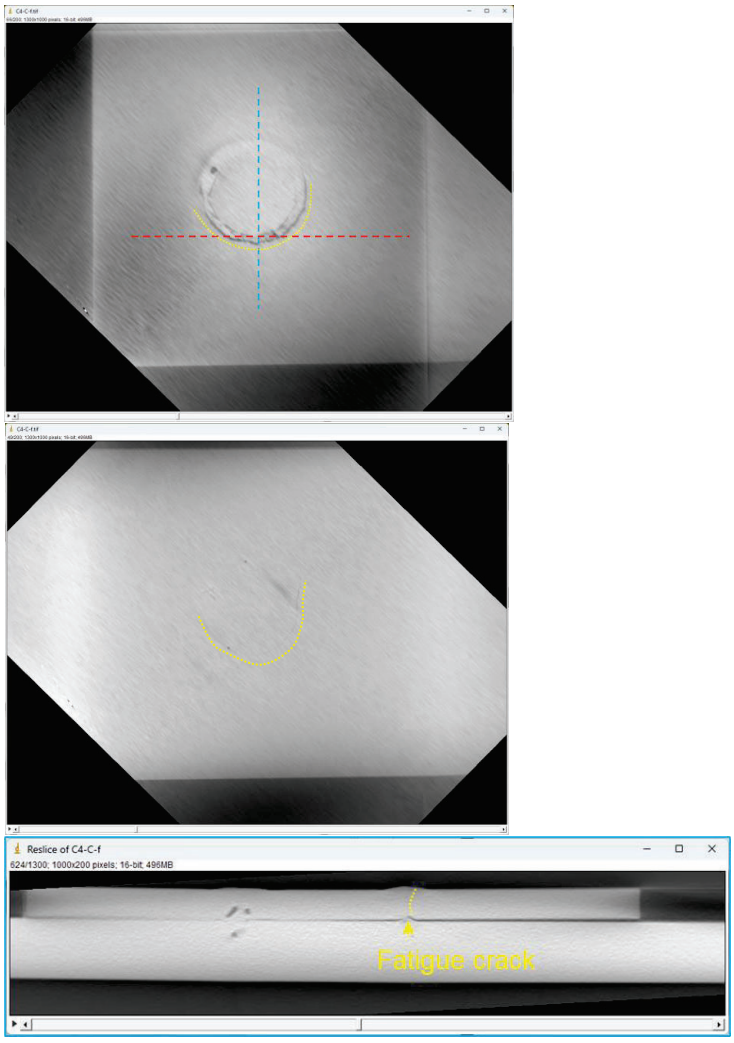
Reslice of C4-C-f
624/1300; 1000x200 pixels; 16-bit; 496MB
Fatigue crack

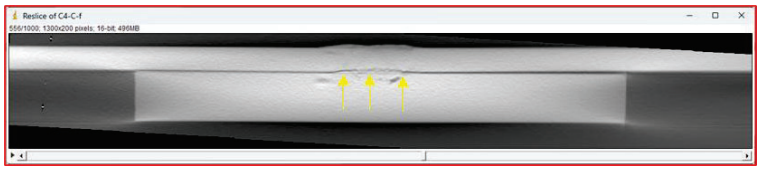

*Figure 43 CT cross-sections from the top in the sheet interface (top), approximately in the middle of the 1050 piece (second from top), transverse vertical (third from top, blue) and transverse horizontal (bottom, red) of the **1 month heat-treated sample** (2 Mcycles, 80 N load amplitude).*

Case 2a – Effect of tin coating thickness (El-Supply)

SEM images of the as-deposited tin coating and the interfaces of the as-welded samples for each of the three tin coating thicknesses are shown in Figure 44-Figure 46. As mentioned in **Error! Reference source not found.**, the tin coating thickness of the samples produced by Provider 1 was much larger than the intended coating thickness (see **Error! Reference source not found.**).

During welding, the pressure applied by the welding electrodes squeezes out some of the coating. The generation of heat leads to the formation of Cu-Sn intermetallic compounds between the tin coating and the copper substrates. From the BSE images in Figure 44-Figure 46, it can be seen that two distinct intermetallic compounds form (as evidenced by the difference in Z-contrast). Investigations performed by other researchers suggest that the intermetallic compound that is richer in Sn is Cu_6Sn_5 while the more Sn-lean intermetallic compound is Cu_3Sn[24].

Commented [TH1]: W. C. W. Ng *et al.*, "Dissolution in service of the copper substrate of solder joints," *2016 IEEE 18th Electronics Packaging Technology Conference (EPTC)*, Singapore, 2016, pp. 388-393

Commented [ES2R1]: La till referensen

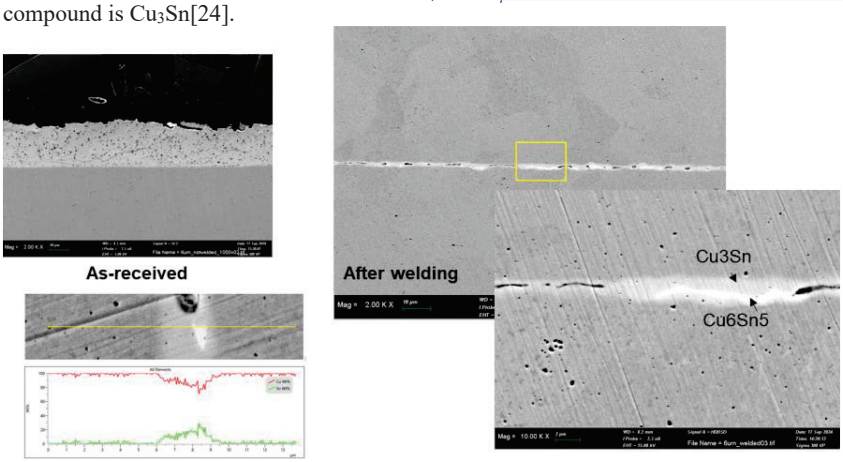

Figure 44 SEM images of the 6 µm tin coating (Provider 1) on the copper before welding (top left) and the intermetallic layer formed between the two coated copper pieces after welding (right). An EDS line scan of the intermetallic layer is shown on the bottom left.

Despite the significant difference in as-deposited tin coating thickness among the three samples, the thickness of the intermetallic layer formed at the interface after welding is approximately 2-3 µm for all three initial tin coating thicknesses; 4 µm to 21 µm (Table 1). However, the amount of Sn-rich Cu_6Sn_5 was qualitatively higher in the case of the thickest tin coating. In all three cases, small discontinuities assumed to be Kirkendall voids were observed in the intermetallic layer.

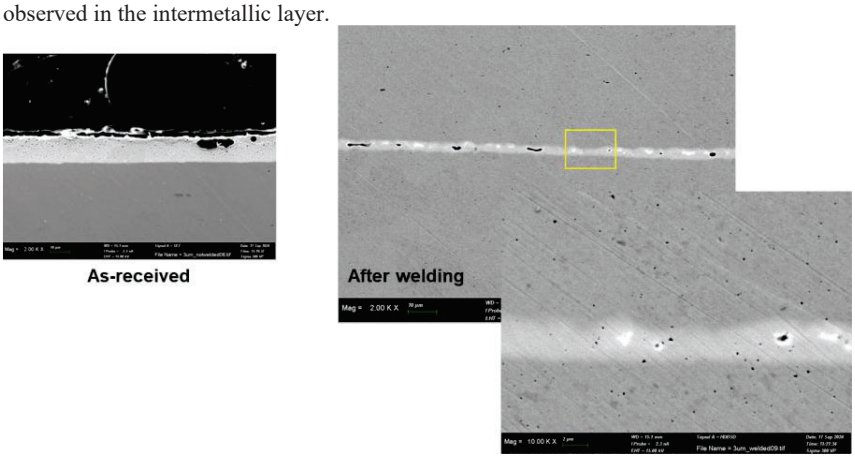

Figure 45 SEM images of the 3 µm tin coating (Provider 1) on the copper before welding (top left) and the intermetallic layer formed between the two coated copper pieces after welding (right).

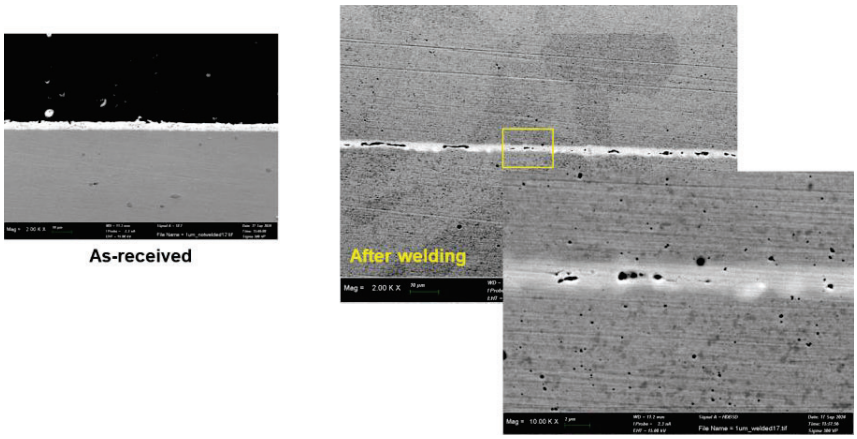

Figure 46 SEM images of the 1 µm tin coating (Provider 1) on the copper before welding (top left) and the intermetallic layer formed between the two coated copper pieces after welding (right).

Table 1 Nominal thickness and measured thickness of the tin coatings (Provider 1) used in this case, and the resulting thickness of the intermetallic layer formed during welding. Measurements of the intermetallic layer were performed in the middle of the weld joint.

Nominal thickness (µm)	***SEM-measured thickness, as-coated (µm)***	***Intermetallic layer after welding (µm)***
1	4.1	2.1
3	13	3.0
6	21	2.3

Cross-tension testing of the as-welded samples were performed at El-Supply. The thinnest nominal coating thickness of 1 µm (actual 4.1 µm) gave a maximum tensile force of 6165.8 N. Increasing the coating thickness to 13 µm produces an approximately 10% improvement in the maximum tensile force, but further increasing the coating thickness to 21 µm results in a 4% decrease in maximum tensile force. In all cases, failure occurred in the base material away from the welded joint. Interestingly, the change in maximum tensile force follows the same trend as the measured intermetallic layer thickness formed during welding. However, since fracture occurred in the base material, the thickness of the IMC layer likely does not have a direct impact on the tensile strength of the joint, but changes in tensile strength and IMC thickness may be related to variations in temperature among the three samples. This potential connection requires further investigation.

Table 2 Nominal coating thickness (Provider 1) and the maximum tensile force exhibited during quasistatic cross-tension testing.

Coating thickness (µm)	***Max. tensile force (N)***
4.1	6165.8
13	6808.2
21	6527.5

Load-displacement curves for the 4.1 µm- and 21 µm-thick tin coating samples from Provider 1 are shown in Figure 47. The hysteresis width for the 4.1 µm-thick coating

Commented [TH3]: IMC tjocklek varierade över mellan mitt och kant, är detta mätt på mitten?

Commented [ES4R3]: På mitten, la till en mening i tabellbeskrivingen

Commented [TH5]: Brott skedde i basmaterialet kan ej bero på IMC

Commented [TH6R5]: Om det är ett samband så kan det vara temperatureffekt som påverkat basmaterialet, men detta kräver mer arbete för att förstå

Commented [ES7R5]: La till några meningar enligt kommentar

sample was observed to gradually increase over the course of the fatigue test, while the 21 μm-thick tin coating sample remained relatively stable at 120 μm hysteresis width throughout the test. These results indicate potentially worse fatigue performance for the thinner coating under these conditions, but the actual thicknesses of the tin coating (approx. 4 μm vs. 21 μm) should also be kept in mind when considering these results.

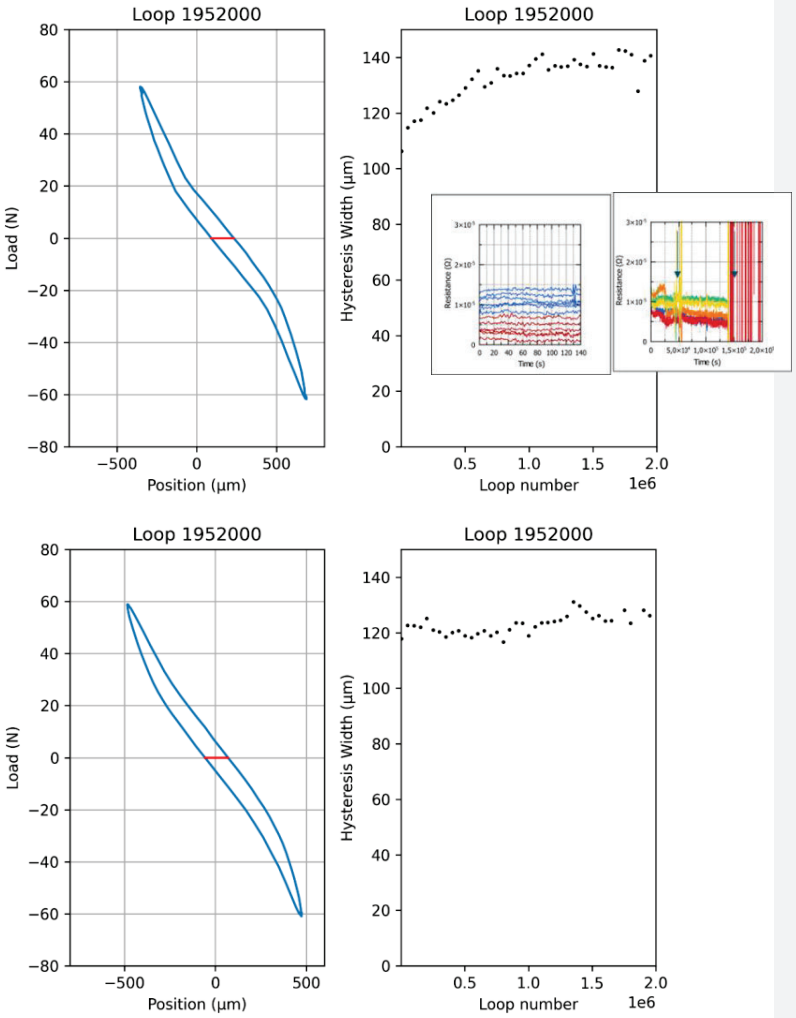

Figure 47 Load vs. displacement loops and hysteresis width for nominal 1 µm-thick tin coating (actual 4.1 µm, Provider 1, top) and nominal 6 µm-thick tin coating (actual 21 µm Provider 1, bottom). 2 Mcycles, 60 N load amplitude. The inset graphs at the top show the voltage drop with and without reversed polarity before testing (left) and the voltage drop during testing (right).

Cross-sections of the 4.1 µm-thick tin coating sample before and after fatigue testing can be compared in Figure 48-Figure 51. Most importantly, examples of fatigue damage can be seen in Figure 50 and Figure 51. Here, fatigue cracks initiated in the thick intermetallic layer that developed near the outer edges of the sample due to the welding electrodes squeezing out the tin coating during welding. However, near the center of the weld joint where the intermetallic layer is much thinner, fatigue cracks were instead observed to initiate at the interface between the intermetallic layer and the copper substrate, after which the cracks propagated further into the copper substrate.

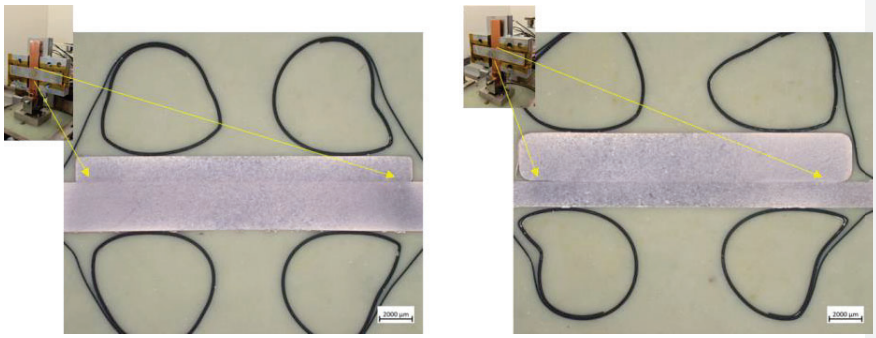

Figure 48 Macro cross-sections of samples with nominal 1 µm-thick tin coating (actual 4.1 µm, Provider 1) as-welded (left) and after 2 Mcycle of fatigue at 60 N load amplitude (right).

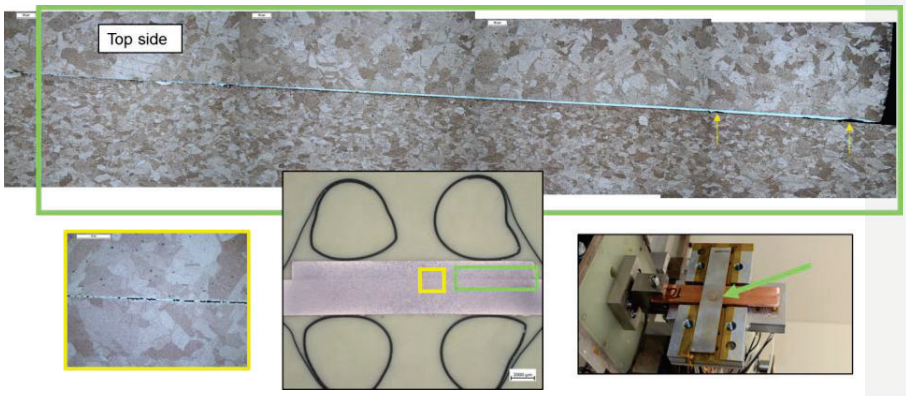

Figure 49 Stitched LOM micrograph of the weld interface for the nominal 1 µm-thick tin coating sample (actual 4.1 µm, Provider 1) in the as-welded condition. Higher magnification micrograph of the weld interface (bottom left). Photograph showing the location of the micrographs (bottom center). Orientation of the sample in the fatigue testing rig (bottom right).

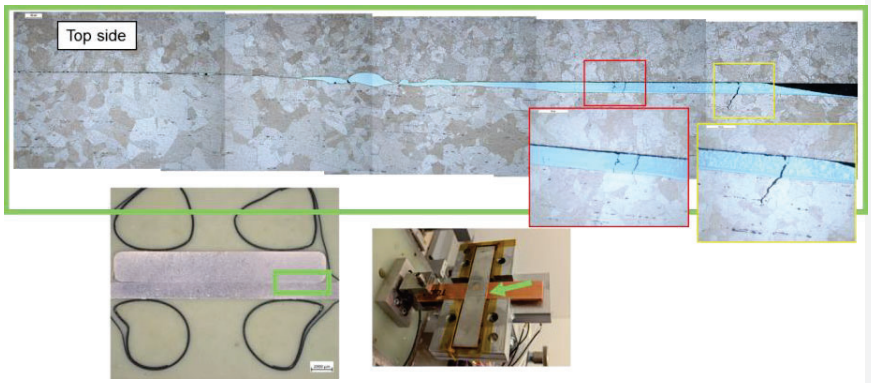

Figure 50 Stitched LOM micrograph of the weld interface for the nominal 1 µm-thick tin coating sample (actual thickness 4.1 µm, Provider 1) after 2 Mcycles, 60 N load amplitude fatigue testing. Higher magnification micrograph of the weld interface (bottom left). Photograph showing the location of the micrographs (bottom center). Orientation of the sample in the fatigue testing rig (bottom right).

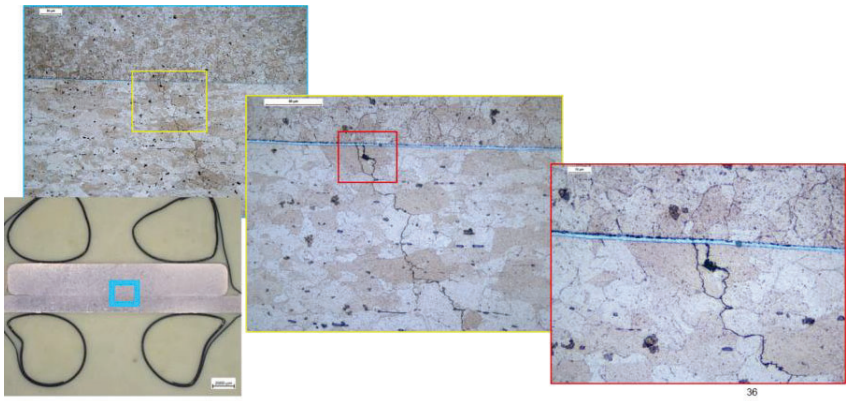

Figure 51 Higher magnification LOM images of the nominal 1 µm-thick tin coating sample (actual thickness 4.1 µm, Provider 1) subjected to fatigue.

1 µm- and 6 µm-thick tin coating samples from Provider 2, which produced tin coating thicknesses closer to the nominal thickness (Table 3), were also subjected to fatigue testing for 2 Mcycles with a 50 N load amplitude. The load-displacement loops for these samples are shown in Figure 52. In this case, the 1 µm coating exhibited a more stable hysteresis

width as opposed to the 6 µm coating. Although the nominal 6 µm coating sample fatigue test had to be restarted at approximately 600 kcycles, evidence of a gradual increasing hysteresis width can still be seen in Figure 52. Interestingly, the actual tin coating thickness of 3.8 µm is similar to the 4.1 µm tin coating thickness of the worse-performing sample (nominal 1 µm coating thickness) produced by Provider 1.

Table 3 Nominal thickness and measured thickness of the tin coatings (Provider 2) used in this case, and the resulting thickness of the intermetallic layer formed during welding. The 3 µm coating sample was not tested or cross-sectioned.

Nominal thickness (µm)	***X-ray-measured thickness, as-coated (µm)***	***Intermetallic layer after welding (µm)***
1	1.3	0.90
3	2.7	--
6	3.8	1.86

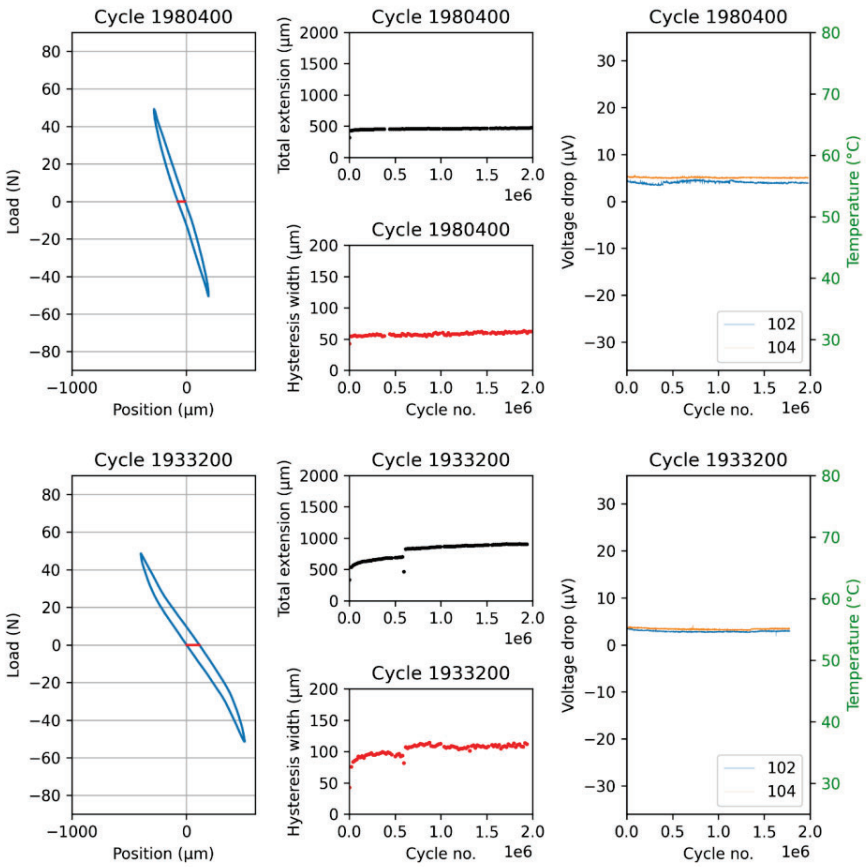

Figure 52 Load vs. displacement loops and hysteresis width for 1 µm-thick tin coating (Provider 2, top) and 6 µm-thick tin coating (Provider 2, bottom). 2 Mcycles, 50 N load amplitude.

Cross-sectioning of the 1 µm coating sample did not reveal any fatigue damage. However, the 6 µm coating sample possessed a clear fatigue crack initiating from the outer edges of the bonded area (Figure 53). The crack appeared to have followed the Cu-Cu interface before branching off into the thicker of the two copper pieces.

Commented [TH8]: 1 mikrometer Sn (1.3 mikrometer) ser ut att vara bäst. Om det är så ska det med i conclusionUtmattningsspricka i IMC för 6 mikrometer Sn.

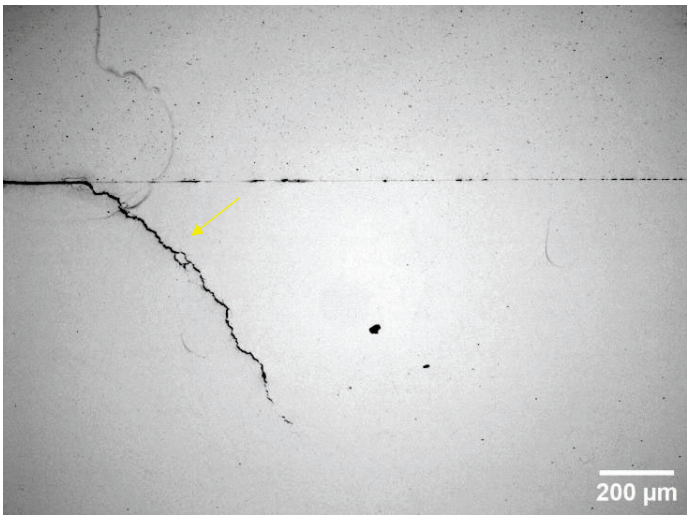

Figure 53 LOM micrograph of the 6 µm coating sample (Provider 2) after fatigue testing for 2 Mcycle at 50 N load amplitude.

Case 2b – Effect of projections (El-Supply)

The intended goal with the use of projections was to eliminate the need for tin-coating, a processing step which is costly in both time and money. Moreover, in some applications tin-coated copper cannot be used. By creating a projection in one of the copper strips to be welded, the welding current should be focused through the smaller cross-sectional area of the projection and increase the extent of Joule heating at the interface between the two copper strips.

Figure 54 shows macro cross-sections of an as-welded sample which used projections. In the center of the welded joint, no visible gap is present between the two workpieces, whereas a small gap near the projections is seen in the cross-section taken from the middle of the projections.

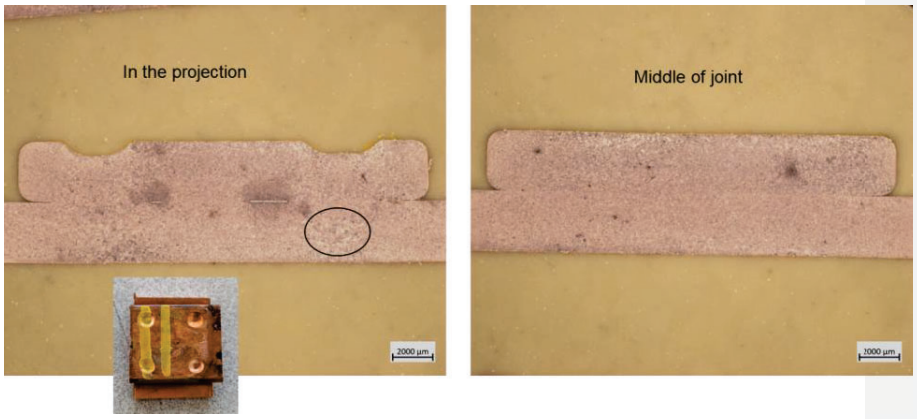

Figure 54 Macro cross-sections of a projection-welded copper sample. The cross-section on the left was taken from the middle of the projections, whereas the cross-section on the right was taken from the middle of the welded joint (see inset photograph).

LOM after etching was used to examine the microstructure of one of the projection welds (Figure 55). Here, grain coarsening was observed in weld-affected zone. Given the absence of any identifiable solidification structure, it is assumed no melting of the copper workpieces occurred during welding.

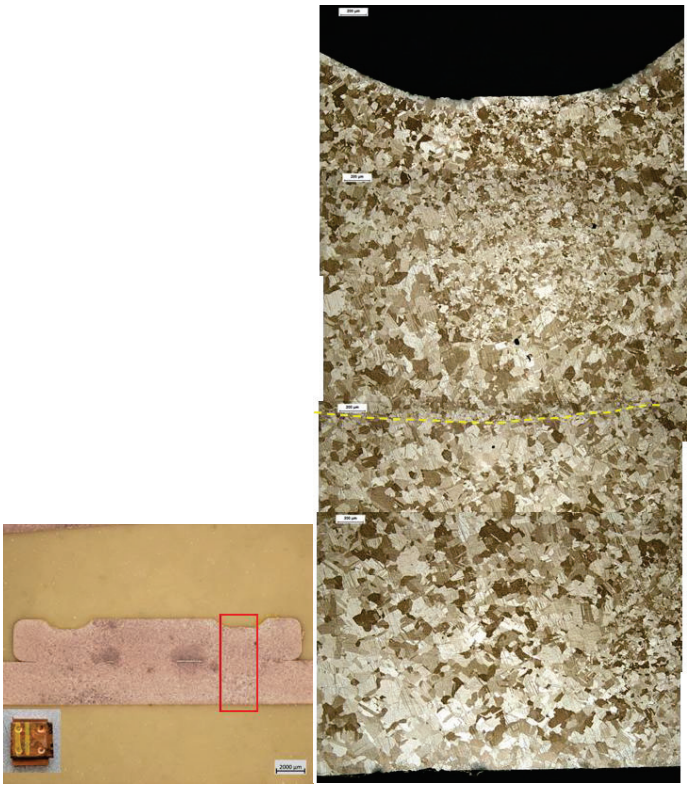

Figure 55 Stitched LOM image (right) of the weld-affected zone in a projection-welded copper sample. The red box in the photograph on the left shows the area of the stitched image.

Higher magnification LOM images of the joint interface are shown in Figure 56. Even in the centre of the projection, a distinct interface was still seen between the two copper strips. However, at higher magnification, some intermittent diffusion bonding appears to have arisen during the projection welding.

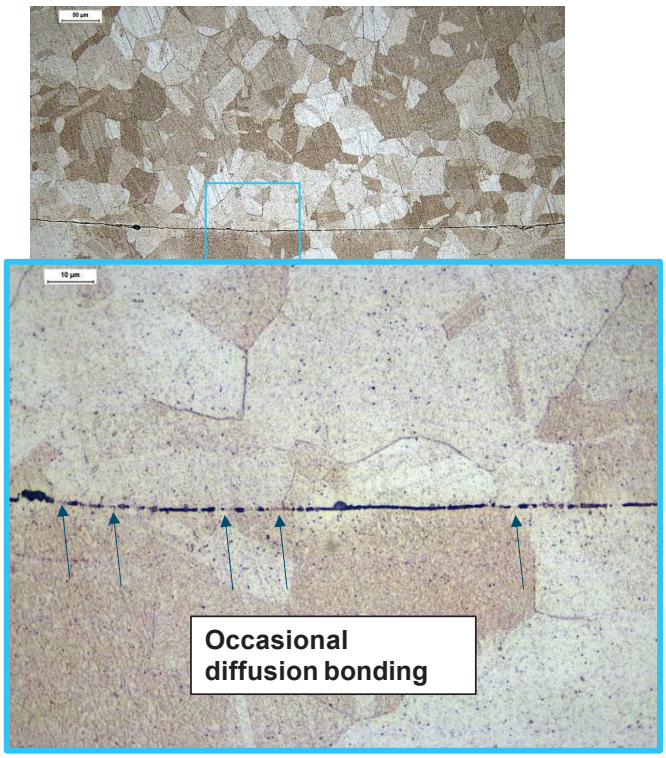

Figure 56 Higher magnification LOM images of the projection weld interface showing indications of the formation of a diffusion bond between the two copper strips.

The maximum tensile force achieved by the projection welded copper samples was 3202 N as compared to a maximum tensile force of 6808.2 N achieved in the tin-coated case. While failure in the tin-coated samples occurred in the base metal, failure of the projection-welded samples occurred interfacially in the welded joint.

Due to time limitations, fatigue testing of these samples could not be performed in this project.

Have the goals been reached?

Technical Goals	*Have the goals been reached*
- Developing a universal method for fast and precise measurements of contact resistance in welded electrical joints. The method should also be able to monitor contact resistance variations for determination of crack initiation. This technique is commonly known as Direct Current Potential Drop (DCPD) but needs to be adapted for the application.	Yes, a fatigue test rig was developed to perform fatigue test under constant current load, as well as a test coupon was proposed to mimic the laser welded aluminum connection in a prismatic battery. In general, detection of fatigue damage via the force-displacement loop was more accurate than via measurement of the voltage drop. In some cases, the voltage drop could be correlated with the presence of fatigue damage, but this correlation was typically not consistent.
- Summarize state of the art techniques and requirements for welding electrical connections. Welding methods, material solutions and recycled alloys and environmental aspects should be included to help manufacturers choose the best method with lowest environmental impact.	yes
- Defining degree of restraint and temperature cycles for busbars to be used as input for demonstrator and FEM simulation.	Yes. The weld starts and especially the weld stops were found to contain more defects compared to the steady-state portion of the weld. Weld starts/stops should therefore be placed in areas that are subjected to lower tensile stresses. FEM was demonstrated to be a useful tool in predicting suitable, low-stress locations on the component.
- Develop models for analysis of fatigue results from standardized specimens and utilize these for optimized design of busbars.	yes
- Developing and verifying a fatigue testing method for standardized test specimens with the ambition to make it	Yes. The clearest indicator of fatigue damage accumulation was provided by the morphology

broadly adopted in the EV industry. The testing method will link the contact resistance, weld geometry, welding process/parameters and busbar geometry.	of load-displacement loop during fatigue testing. As the fatigue test progressed, the load-displacement loop became markedly more asymmetric, and both the total extension and hysteresis width steadily increased until the autostop threshold was reached. The hysteresis width of a load-displacement loop is attributed to the energy dissipated by the sample for that cycle. As fatigue damage accumulates, the width of the hysteresis loop increases From this study, samples exhibiting a steady hysteresis width throughout the duration of the fatigue test typically had no or minimal fatigue damage.
- With a demonstrator showing the full work methodology going from a CAD drawing of a busbar to verifying if the construction will reach targeted fatigue performance.	No, this had to be postponed to the next project.
- To ensure high performance of the electrical joints in the battery pack which will increase the power efficiency, reduce risk of breakdowns, and extend the lifetime of the vehicle.	Yes.

Sustainability/circularity Goals

Have the goals been reached?

-	*Have the goals been reached*
- Through the development of a new fatigue testing method enable manufacturers to compare, test and	yes

	qualify recycled alloys for use in battery pack construction to increase circularity and minimize environmental impact.	
-	To ensure high performance of the electrical joints in the battery pack which will increase the power efficiency, reduce risk of breakdowns, and extend the lifetime of the vehicle.	yes
-	To minimize the carbon footprint of EVs by enabling long life and 2nd life opportunities of the battery pack.	yes
-	Enable manufacturers to maximize the lifetime of the product and review changes in the material, process, or geometry.	yes

7. Dissemination and publications

7.1 Dissemination

How are the project results planned to be used and disseminated?	Mark with X	Comment
Increase knowledge in the field	X	
Be passed on to other advanced technological development projects	X	
Be passed on to product development projects	X	
Introduced on the market		
Used in investigations / regulatory / licensing / political decisions		

7.2 Publications

Swerim report : Report COMMIT Swerim-2025-240
Part of the result was presented at Laserdagen I, Älvsjö 2025-05-06 "**Electric joints optimized for increased thermal and mechanical fatigue life"**

8. Conclusions and future research

This study was mainly aimed at developing a new testing methodology for investigation of thermal and mechanical fatigue in laser welded busbar-tab (Al 1050 to Al 3003) electrical connections in prismatic battery cells. Additionally, evaluation of permanent electrical connections for other applications was included in this study to broaden the use of the developed test method. Thus, laser welded busbars of Al 1370 to Al 3003 and Al 6101 to Al 3003 as well as resistance welded tin coated copper busbars were included in this study.

Based on the experiments performed in this study the following conclusions have been reached for laser welded aluminum busbar-tabs:

- Test method – In general, detection of fatigue damage via the force-displacement loop was more accurate than via measurement of the voltage drop. In some cases, the voltage drop could be correlated with the presence of fatigue damage, but this correlation was typically not consistent. High-resolution X-ray computed tomography (CT) was an effective method for detecting welding defects such as gas pores or solidification cracks.

- Fatigue performance – Overall, the majority of samples survived intermediate- or high-cycle fatigue testing at high load amplitudes despite the presence of weld defects like gas pores or solidification cracks.
- Effect of mechanical fatigue under constant current load – With an applied 300 A, samples experienced an increase in temperature typically between 40 °C – 60 °C depending on the weld geometry. With the small temperature increase, a clear decrease in fatigue performance was not seen from the application of high current alone. Potentially worse fatigue performance was seen in the Volvo Cars samples that were heat-treated 1 month at 120 °C.
- Effect of end crater – In general, the abrupt cessation of laser power in the weld stop gives rise to an end crater region that possesses defects like gas pores and solidification cracks. The solidification cracks in particular were observed via CT to act as initiation points for fatigue damage.
- In the case where solidification cracks exist, pores seem to be less important for crack initiation.
- Effect of oxidation (simulating one year storage at RT, 100% RH) – An increase in the oxide layer thickness from approximately 2 -3 nm to approximately to 9 - 10 nm, contributed to the formation of larger pores at the sides of the weld, which is likely undesirable for fatigue performance.
- Effect of annealing (350 °C, 1 hour) combined with a small gap resulted in almost pore-free welds. However, further research is needed to conclude this. The soft-annealed samples survived for a high-cycle severe fatigue testing at very high-load amplitude despite a less-than-optimal microstructure caused by the annealing (i.e. significant recrystallization and grain growth). Annealing has the potential to reduce the mechanical stress on the joint caused by the forces transferred by the busbar.
- The soft-annealing heat treatment performed before laser welding likely induced significant recrystallization and grain growth in the initially cold-rolled samples, and more extensive fatigue damage was observed by CT. However, the soft-annealed samples survived for a long-time severe fatigue testing at very high load amplitude despite a less optimal microstructure caused by the annealing. An interesting side effect of the annealing treatment was a reduction in gas pores in the as-welded condition.
- Effect of different Al alloys – A higher extent of solidification cracking in the end crater and in the steady-state portion of the weld was observed in 6101-3003 laser-welded samples.
- Effect of weld shape – The weld geometry plays a large role in dictating where cracks initiate and propagate. In the linear welds, cracks were nearly always found to initiate at solidification cracks in the end crater and then propagate along the weld length while remaining wholly in the 1050 tab material.
- Effect of weld width – Decreasing weld width of linear welds from 1.0 mm to 0.7 mm has a noticeable, detrimental effect on fatigue performance.

And for resistance welded tin coated copper busbars the following conclusion can be drawn:

- The resistance welded tin coated copper with a 2-3 µm thick intermetallic phase between the two resistance welded copper busbars, withstood severe fatigue test for an intermediate cycle fatigue test at a high load amplitude despite cracks in the intermetallic compound (2 Mcycles, 60 N load amplitude). In locations where the IMC was thicker, such as the outer edges of the weld, some fatigue damage was observed to initiate within the intermetallic compound and propagate a short distance into the copper base material.
- For coating thicknesses above 3 µm, the thickness of the intermetallic compound formed during welding was almost the same regardless of the thickness of the tin coating.
- Of the samples produced with an accurate coating thickness (Provider 2), a nominal coating thickness of 1 µm (actual thickness 1.3 µm) gave a more stable fatigue performance compared to nominal 6 µm coating thickness (actual thickness 3.8 mm). Thus, the optimum tin coating thickness is probably in the range of 1 – 3 µm.

An important consideration for designing future investigations is to take into account differences between the lab-scale weld samples, like those produced in this work, compared to the laser welds made in the production environment. Specifically, the samples in this work are longer with more mass, which may change the thermal profile experienced by the material during welding. The shorter tabs used in production are shorter and lie in a plastic tub during welding. The accidental introduction of gaps due to misalignment and the use of oil during punching and forming are also factors that arise during production. For further verification and to raise the TRL of future projects, testing on the module-level in a quasi-production environment is recommended.

Moreover, it should be noted that investigation of fatigue, which is a highly defect-controlled failure mechanism, requires testing of several duplicate samples in order to draw conclusions with statistical confidence

Several new projects are looking further into different aspects regarding laser weld quality, quality assurance and standardization, and alternative joining techniques; these projects are listed below.

- CODELAB “Vinnova diary number 2025-00824” – requirements/standards for defects in laser-welded aluminium
- SAFEMODE – expanded experimental investigation based on findings in CODELAB
- SOLSTA – prestudy to investigate solid-state joining techniques for electrical and BiW applications
- Cylindrical cells – dissimilar material combinations
- Laser welding Cu-Cu

9. Participating parties and contact persons

El-supply i Ed AB	Robert van Brakel
Lasertech LSH AB	Elias Repper
Hydro Extruded Solutions AB	Jonas Kristoffer Sunde
Northvolt Systems AB	Karl Fahlström
Scania CV AB	Therese Källgren
Swerim AB	Tag Hammam, Ethan Sullivan
Volvo Car AB	Daniel Andersson, Albin Knutsson